



Universität Hamburg

DER FORSCHUNG | DER LEHRE | DER BILDUNG

Sensitivity Studies for the THEIA Experiment at LBNF

Sensitivitätsstudien für das THEIA- Experiment an LBNF

Thesis

for the Degree of Master of Science in Physics

at the

Fakultät für Mathematik, Informatik und Naturwissenschaften

Fachbereich Physik

Universität Hamburg

by

Wei-Chieh Lee

born on

13 February 1996 in New Taipei City, Taiwan

First reviewer: Dr. Daniel Bick

Second reviewer: Prof. Dr. Michael Wurm

Submitted in 2023

Abstract

THEIA is a next-generation neutrino detector, which can achieve great precision in neutrino event reconstruction and background rejection by exploiting both Cherenkov radiation and scintillation light. With this type of detectors, the nature of neutrinos may be further investigated to provide answers to unsolved questions in physics, especially those of the mass ordering and the possible CP violation in neutrino oscillations. For this purpose, the detector is proposed to be constructed at the Long-Baseline Neutrino Facility (LBNF) in the United States, measuring the neutrinos that underwent oscillation during their travel through the Earth. In this thesis, the General Long Baseline Experiment Simulator (GLOBES) software package has been utilized for the experiment performance simulation. Studies of THEIA's ability to discover CP violation are presented with details, including effects from variations in oscillation parameters and experimental uncertainties. In addition, a brief presentation of THEIA's sensitivity to determine the neutrino mass ordering is included. With conservative assumptions on the detector's performance and a 7-year neutrino beam exposure, THEIA-100 can ultimately have $> 3\sigma$ ($> 5\sigma$) sensitivity to CP violation for 60% (20%) of δ_{CP} parameter space in the case of true normal (inverted) mass ordering. THEIA-25, on the other hand, has a comparable sensitivity to that of a 17.1-kt far detector (FD) of the Deep Underground Neutrino Experiment (DUNE), and therefore is one of the detector options currently discussed for the module of opportunity in the second phase of DUNE. As for the determination of neutrino mass ordering, both THEIA-25 and THEIA-100 can achieve a $\sqrt{\Delta\chi^2} > 5$ significance for all of the δ_{CP} parameter space.

Zusammenfassung

THEIA ist ein Neutrinodetektor der nächsten Generation, der eine hohe Präzision bei der Rekonstruktion von Neutrinoereignissen und der Hintergrundunterdrückung erreichen kann, indem er von sowohl Tscherenkow-Strahlung als auch Szintillationslicht Gebrauch macht. Mit dieser Art von Detektoren kann die Natur von Neutrinos weiter untersucht werden, um Antworten auf ungelöste Fragen der Physik zu geben, insbesondere solche der Massenordnung und der möglichen CP-Verletzung in Neutrinooszillationen. Zu diesem Zweck soll der Detektor an der Long-Baseline Neutrino Facility (LBNF) in den Vereinigten Staaten gebaut werden, um die Neutrinos zu messen, die während ihrer Reise durch die Erde oszilliert haben. In dieser Abschlussarbeit wurde das Softwarepaket General Long Baseline Experiment Simulator (GLOBES) für die Simulation der Experimentleistung verwendet. Studien über die Fähigkeit von THEIA, eine CP-Verletzung zu entdecken, werden mit Details vorgestellt, einschließlich Auswirkungen von Variationen in Oszillationsparametern und experimentellen Unsicherheiten. Darüber hinaus ist eine kurze Vorstellung von der Sensitivität von THEIA zur Bestimmung der Neutrino-Massenordnung enthalten. Mit konservativen Annahmen zur Leistung des Detectors und einer 7-jährigen Aufnahme des Neutrinostrahles kann THEIA-100 letztendlich eine Sensitivität von $> 3\sigma$ ($> 5\sigma$) bezüglich der CP-Verletzung für 60 % (20 %) des Parameterbereichs von δ_{CP} aufweisen, wenn die normale (inverse) Massenordnung realisiert ist. THEIA-25 hingegen hat eine vergleichbare Sensitivität wie ein 17,1 kt schwerer Ferndetektor (FD) des Deep Underground Neutrino Experiment (DUNE) und ist daher eine der Detektoroptionen, die derzeit für das Modul der Möglichkeit in der zweiten Phase von DUNE diskutiert werden. Zur Bestimmung der Neutrino-Massenordnung können sowohl THEIA-25 als auch THEIA-100 eine Signifikanz von $\sqrt{\Delta\chi^2} > 5$ für den gesamten Parameterbereich von δ_{CP} erreichen.

Table of Contents

INTRODUCTION	1
CHAPTER 1 Neutrino Physics	3
1.1 Neutrinos as Part of the Standard Model	4
1.1.1 Weak Interaction	5
1.1.2 CP-Symmetry	7
1.2 Neutrino Oscillation	8
1.2.1 MSW Effect	10
1.2.2 Oscillation Parameters	11
1.3 Open Questions	13
1.3.1 Precise Measurement of Oscillation Parameters	13
1.3.2 Neutrino Mass	14
1.3.3 Majorana Neutrino	15
1.3.4 Sterile Neutrino	16
CHAPTER 2 Neutrino Detection with THEIA	19
2.1 Detection Principles	19
2.2 Detection Techniques	20
2.2.1 Scintillation	20
2.2.2 Cherenkov Radiation	21
2.2.3 Photo-Detection	24
2.3 THEIA Detector	26
2.3.1 Detector Concept	27
2.3.2 Realization in a Long-Baseline Experiment	28

CHAPTER 3 Long-Baseline Neutrino Oscillation Experiment	29
3.1 Experiment Description	30
3.1.1 Neutrino Beam Production	30
3.1.2 Baseline	33
3.1.3 Detector Performance	33
3.2 Experiment Simulation	35
3.2.1 Oscillation Channels	36
3.2.2 Simulated Event Rate	38
CHAPTER 4 Simulation Data Analysis	41
4.1 Analysis Procedure	41
4.1.1 Oscillation Parameter Uncertainties	42
4.1.2 Systematic Uncertainties	43
4.1.3 Hypothesis Testing	44
4.2 Result: Sensitivity to Leptonic CP Violation	46
4.2.1 Effect of Different Oscillation Parameter Assumptions	48
4.2.2 Effect of Variation in Experimental Uncertainties	50
4.3 Result: Sensitivity to Neutrino Mass Ordering	51
CONCLUSION	55
LIST OF ABBREVIATIONS	57
BIBLIOGRAPHY	61
ACKNOWLEDGEMENTS	67

Introduction

Neutrinos are so fascinating. Throughout the development of particle physics, there exists no other elementary particle that is as mysterious as the neutrinos. They are loners, hardly engaging interactions with others. They are everywhere, coming from every part of the universe, far as the Big Bang and close as within the Earth. They are extremely light, and change their appearance constantly as they travel, fooling the minds that cannot comprehend their complexity. Yet, by following them, they will lead you to the answers to a much greater mystery that is our universe. There will be more stories for these particles to tell for sure, as every physicist, every experiment on Earth listens very carefully to these tiny little messengers that deliver the knowledge of the universe to us.

The neutrinos, as we know them today, are neutral leptons that can be categorized into three types (flavours): electron neutrino (ν_e), muon neutrino (ν_μ) and tau neutrino (ν_τ), each named correspondingly to their charged partner leptons. As part of the Standard Model (SM) of particle physics, neutrinos participate solely in the weak interaction mediated by W and Z bosons. Since neutrinos are neutrally charged, their detection can only be achieved by observing the charged products from their interaction with the detector medium. So was their existence confirmed in the experiment conducted by Clyde L. Cowan and Frederick Reines in 1956.

The oscillation nature of the neutrinos, however, was not known until the 1960s, when the Homestake experiment conducted by Raymond Davis, Jr. and John N. Bahcall discovered a deficit in the amount of neutrinos expected from the Sun. As Bruno Pontecorvo later suggested, the neutrinos have the ability to change flavours whilst in flight, which constitutes the root of this solar neutrino problem. This nature is then observed and studied by several neutrino experiments, where the measurement of the oscillation parameters introduced by the

Pontecorvo–Maki–Nakagawa–Sakata (PMNS) matrix has the highest priority. So far, most of the parameters have been determined with great precision, with the exception of the θ_{23} octant, the CP-violating phase δ_{CP} and the sign of the atmospheric mass-squared difference, also known as the neutrino mass ordering. The THEIA experiment, introduced with this thesis, aims exactly to measure those parameters, especially the δ_{CP} and the mass ordering.

THEIA, a combination of water Cherenkov detector (WCD) and liquid scintillator (LSc) detector, is a new-generation neutrino detector that has the ability to extract information of the detected neutrinos using both Cherenkov and scintillation light. The newly developed water-based liquid scintillator (WbLS) is its detector body, and the ultrafast-timing Large Area Picosecond Photo-Detectors (LAPPDs) with the conventional photomultiplier tubes (PMTs) cover THEIA to detect the light signals from the detector body. Such a detector is expected to have a great performance in neutrino event reconstruction. With its help, the so far unknown oscillation parameters may finally be determined.

For this purpose, THEIA is proposed to be constructed in connection with the Long-Baseline Neutrino Facility (LBNF) hosted by the Fermi National Accelerator Laboratory (Fermilab). This facility utilizes the accelerator neutrinos coming from Fermilab to conduct an experiment on neutrino oscillation. THEIA is placed 1,300 km away from the neutrino source, detecting the oscillated neutrinos. Such a long baseline serves to increase the experiment's ability to detect the difference in the oscillation probabilities between neutrinos and antineutrinos due to the CP violation in the lepton sector and the matter effect.

As this experiment is not yet realized, a simulation of the experiment has to be performed for the study of its potential. In this thesis, the General Long Baseline Experiment Simulator (GLOBES) is utilized for such a simulation, where the experiment environment at LBNF and the detector performance of THEIA can be described to show the expected results of detection. With the help of this simulation software, the sensitivity of THEIA to CP violation and neutrino mass ordering is then revealed to demonstrate the detector's potential.

In this thesis, the theories relating to neutrinos, neutrino oscillation and the open questions are introduced in Chapter 1. In Chapter 2, the neutrino detection principles and techniques with a final focus on the THEIA detector are presented. As for the neutrino oscillation experiment with THEIA, the LBNF is described in detail, and the simulation method is introduced in Chapter 3. Finally, the analytic procedure to produce detector sensitivity results is presented in Chapter 4, as well as the complete results of the sensitivity studies for the THEIA experiment at LBNF.

Chapter 1

Neutrino Physics

The name *neutrino* was coined in the Italian language, meaning “little neutral one.” It describes what one would expect at first from this new type of particles, that are very light (or even massless) and electrically neutral. It was proposed at first under the name *neutron* by Wolfgang Pauli [1] to solve a long debate between physicists, that, because the energy spectrum of electrons from beta decay would show a continuous feature rather than a discrete one, it violated the energy conservation law and created a problem in its explanation. But with the introduction of neutrinos, the energy conservation law may be ensured in that neutrinos are emitted alongside electrons during beta decay, and so account for the missing energy from the process. According to the description of Enrico Fermi’s paper on beta decay [2], the process including neutrinos (later known to be *electron antineutrinos*) can be written as:



Since the introduction of this new-proposed particle, it became one of the priorities of experimental particle physicists to detect such a particle and prove its existence. It is then reasonable to assume that one can use the inverted reaction of neutrino production, namely the *inverse beta decay* (IBD),



as the detection method. So Clyde L. Cowan and Frederick Reines conducted such an experiment in 1956 with great success [3]. Reines was later awarded a Nobel Prize in Physics in 1995 for the detection of neutrino [4].¹

¹ Cowan died in 1974, and therefore couldn’t have taken the prize as Nobel Prizes are only awarded to the living.

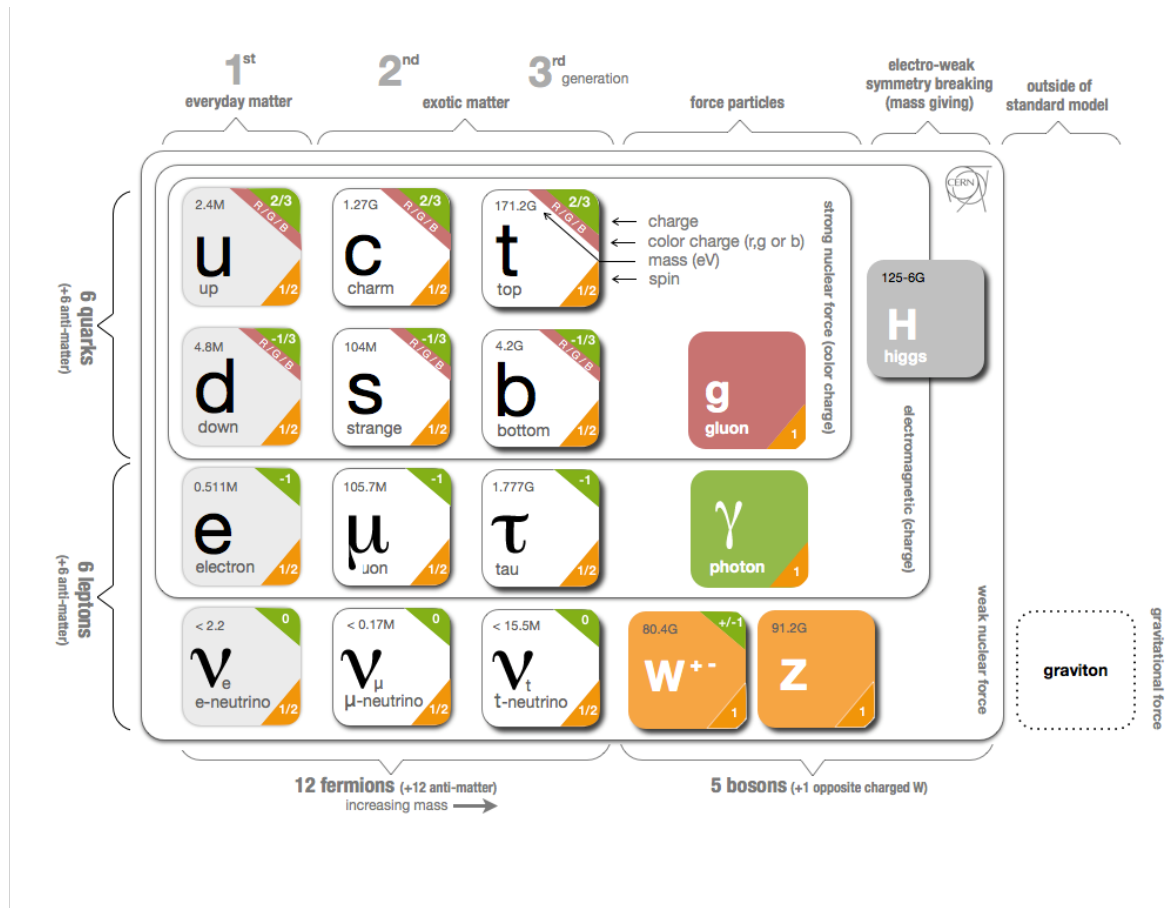


Figure 1.1 – Elementary particles of the Standard Model [5]

Please note that the graviton listed here is only a hypothetical gauge boson mediating the gravitational interaction that does not belong to the Standard Model.

1.1 Neutrinos as Part of the Standard Model

Neutrinos were incorporated into the Standard Model (SM) of particle physics, where there are three types (so-called *flavours*) of neutrinos: electron neutrino (ν_e), muon neutrino (ν_μ) and tau neutrino (ν_τ), each named correspondingly to their partner leptons. All the elementary particles that constitute the Standard Model are displayed in Figure 1.1. The current consensus on three neutrino flavours is then based on several collider experiments and, most notably, the decay of Z bosons into neutrinos and their antineutrinos [6]. These three are the so-called *light neutrinos*, i.e. neutrinos whose mass is less than half the mass of a Z boson. If more flavours of neutrinos were to exist, they would have to be heavier than $m_Z/2$.

Observing the interaction of neutrinos, one can categorize this interaction type as a weak interaction with the exchanging of the W or the Z boson. And since neutrinos don't carry any electric or colour charge, they don't participate in electromagnetic and strong interactions, leaving weak interaction as the only method to detect neutrinos within the theoretical

framework of the Standard Model. The mass of neutrinos, however, is not so obvious in the Standard Model. Physicists have been debating on the subject for the last few decades, but the experiments so far haven't been able to measure it. Consequently, neutrinos were considered massless particles prior to the proposal of neutrino flavour oscillation (see Section 1.2).

1.1.1 Weak Interaction

This subsection serves only to introduce some fundamental properties of weak interaction relating to neutrinos, without describing thoroughly the whole gauge theory of weak interaction.

The weak interaction can be divided into *charged-current (CC) interaction* and *neutral-current (NC) interaction*. The names indicate whether the current formed by the weakly interacting particles has nonzero or zero electric charge. Therefore, it is sufficient to say that CC and NC interactions are distinguished by their mediator bosons, namely W^\pm and Z^0 bosons respectively. As a result, only CC interaction would involve the coupling between neutrinos and their partner leptons, and NC interaction would only be able to deflect neutrinos. This is an important information on how to detect and recognize possible neutrino events in the detectors presented in Chapter 2.

Unlike the electromagnetic and strong interactions, weak interaction treats particles differently due to their handedness, which may be simply illustrated in Figure 1.2:

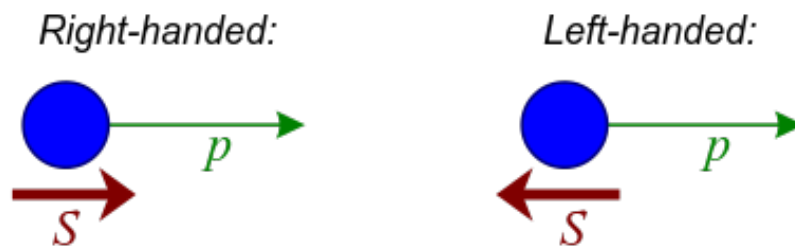


Figure 1.2 – If the spin (S) of a particle is parallel to its momentum (p), the particle is defined as “right-handed.” And if the spin is antiparallel to the momentum, the particle is “left-handed.” [Z]

At this point, it is important to introduce the concept of helicity and chirality: *helicity* is the mathematical form of handedness and is defined by the projection of spin onto momentum. A right-handed spin-1/2 particle would have helicity of $+1/2$; and left-handed $-1/2$. Since helicity is determined by the direction of motion of the particle, the observer may always move to a different reference frame that is faster than the particle to discover the sign of

helicity flipped. In this sense, helicity is not a Lorentz invariant quantity, except for massless particles, where they move in the speed of light and no real observer can move faster than they do.

Chirality, on the other hand, is a more abstract representation of handedness that is Lorentz invariant. It is defined to be the eigenvalue to the eigenstate of operator γ^5 . By using a pair of projection operators, any Dirac field (quantum field of spin-1/2 fermions) can be divided into the “left- and right-handed”² components. Those operators can be written as

$$P_R = \frac{1 + \gamma^5}{2} \text{ and } P_L = \frac{1 - \gamma^5}{2}, \text{ where} \quad (1.3)$$

$$\gamma^5 \equiv i\gamma^0\gamma^1\gamma^2\gamma^3 = \begin{pmatrix} 0 & 0 & 1 & 0 \\ 0 & 0 & 0 & 1 \\ 1 & 0 & 0 & 0 \\ 0 & 1 & 0 & 0 \end{pmatrix}, \quad (1.4)$$

and the Dirac matrices here are $\gamma^0 = \sigma^3 \otimes I$ and $\gamma^j = i\sigma^2 \otimes \sigma^j$ ($j = 1, 2, 3$), where \otimes represents the Kronecker product and σ^j are the Pauli matrices. Subscripts “R” and “L” stand for “right-” and “left-handed” respectively.

Weak interaction treats particle differently due to their chiral handedness. Only left-chiral fermions and right-chiral antifermions participate in CC weak interaction. And in NC interaction, there’s also a clear preference for left-handed chirality over the right-handed one. (And to antiparticles, as always, the opposite handedness applies.) This property can be perfectly described by the symmetry group $SU(2)_L \otimes U(1)$ [8], where all the participating particles can be grouped into doublets and singlets:

Table 1.1 – Particles participating in weak interaction

In each doublet, particles couple to each other. The primes in the quark doublets denote that they have been Cabibbo-rotated. All singlets don’t participate in CC interaction. This table is true also for antiparticles given that the handedness is opposite.

Fermions	Doublets	Singlets
Quarks	$\begin{pmatrix} u \\ d' \end{pmatrix}_L, \begin{pmatrix} c \\ s' \end{pmatrix}_L, \begin{pmatrix} t \\ b' \end{pmatrix}_L$	$u_R, d_R, c_R, s_R, t_R, b_R$
Leptons	$\begin{pmatrix} \nu_e \\ e \end{pmatrix}_L, \begin{pmatrix} \nu_\mu \\ \mu \end{pmatrix}_L, \begin{pmatrix} \nu_\tau \\ \tau \end{pmatrix}_L$	e_R, μ_R, τ_R

² Note that here the concept of handedness is different from that defined by helicity, except for massless particles. In order to differentiate them better, the name “left- and right-chiral” or “chiral left- and right-handed” will be used.

Not included here are the right-handed neutrinos and left-handed antineutrinos, since no observation of these has been shown. Therefore, they are excluded from the weak interaction (consequently the whole Standard Model) and are thought not to exist in the first place. This preference of chirality is a strange property of weak interaction and neutrinos, since it would mean violating a group of universal symmetry laws that are true for the rest of the Standard Model.

1.1.2 CP-Symmetry

The purpose of investigating symmetries in physics theories is to reduce the amount of work to be done. If the theory of a particle interacting is the same as that of an antiparticle one, there's no need to create two theories but to write only one and apply an appropriate symmetry. Thus, constructing a symmetry law that applies to every physical phenomenon is in great interest of the physics community. And in the field of particle physics, the most mentioned symmetries are charge conjugation symmetry (C-symmetry), parity symmetry (P-symmetry) and time reversal symmetry (T-symmetry)³.

P-symmetry suggests that the laws of physics would be left unchanged when all the spatial coordinates are reversed in sign, or in their so-called “mirrored images,” i.e.

$$\mathbf{P} : \begin{pmatrix} x \\ y \\ z \end{pmatrix} \mapsto \begin{pmatrix} -x \\ -y \\ -z \end{pmatrix}. \quad (1.5)$$

This symmetry suffices for physics in electromagnetic and strong interactions [9]. However, the P-symmetry is violated in the weak interaction because of its aforementioned preference on the particle's chirality.

Charge conjugation is essentially a transformation between particles and their antiparticles (i.e. reversing the signs of all “internal” quantum numbers), so by introducing *C-symmetry*, it is suggested that the laws of physics would not change when all the particles are instantly exchanged with their antiparticles, and antiparticles with their particles. But again, C-symmetry is only true in the sector of electromagnetic and strong interactions, not true in the weak interaction for the same reason for P violation. Now, a universal symmetry law of weak interaction is urgently needed.

A combination of C- and P-symmetries, *CP-symmetry*, restores its validity in weak interaction, for a CP-symmetric counterpart of a left-chiral fermion, for example, would be its antifermion of right-handed chirality, both of which behave the same way under weak interac-

³ *T-symmetry* states that the laws of physics would remain the same when time is reversed.

tion. At this stage, CP-symmetry was widely considered to be the true universal symmetry. However, CP-symmetry could not hold for long after some observations of meson decays clearly violated it [1], though still being very close to a symmetry. The question is now also open for the lepton sector, which may be manifested by the different flavour oscillation rate between neutrinos and antineutrinos (see Subsection 1.3.1). (It might be that they are different after all.) Should this be the case, it might just be the answer to one of the fundamental questions of the universe—matter–antimatter imbalance.

1.2 Neutrino Oscillation

By the 1960s, particle physicists were already using these weakly interacting particles as the probing method of various cosmic objects, including the Sun. The Homestake experiment conducted by Raymond Davis, Jr. and John N. Bahcall [10] made measurements of electron neutrinos coming from the Sun, as this was proposed in the Standard Solar Model, in order to investigate the nuclear fusion reactions in the Sun. However, a problem arose when several experiments failed to detect as many neutrinos as predicted in theory. This solar neutrino deficit would be explained by introducing a possibility of neutrinos transitioning from one flavour to another while propagating. This is now known as *neutrino oscillation*.

The physics of neutrino oscillation has been developed by physicists Jiro Maki, Masami Nakagawa, Shoichi Sakata and Bruno Pontecorvo, and is described by a mixing between the flavour eigenbasis and mass eigenbasis:

$$|\nu_\alpha\rangle = \sum_i U_{\alpha i}^* |\nu_i\rangle, \quad (1.6)$$

$$|\nu_i\rangle = \sum_\alpha U_{\alpha i} |\nu_\alpha\rangle, \quad (1.7)$$

where $\alpha = e$ (electron), μ (muon) or τ (tauon) is the flavour of neutrino and $i = 1, 2, 3$ denotes three mass eigenstates with distinct mass m_i . The mixing is represented by a 3×3 unitary matrix $U_{\alpha i}$, the *Pontecorvo–Maki–Nakagawa–Sakata* (PMNS) matrix:

$$U = \begin{bmatrix} U_{e1} & U_{e2} & U_{e3} \\ U_{\mu1} & U_{\mu2} & U_{\mu3} \\ U_{\tau1} & U_{\tau2} & U_{\tau3} \end{bmatrix}. \quad (1.8)$$

This matrix has 9 degrees of freedom, as any general $n \times n$ unitary matrix has n^2 degrees of freedom. These are 3 angles and 6 phases. After reabsorbing some phases through redefinition of the lepton fields [11], the PMNS matrix is left with 4 free parameters, i.e. 3 mixing

angles (θ_{12} , θ_{23} and θ_{13}) and one CP-violating phase δ_{CP} , here assuming that neutrinos are Dirac particles (see Subsection 1.3.3). It can then be written in the fashion of rotation matrices between every two flavour eigenstates and every two mass eigenstates as:

$$U = \begin{bmatrix} 1 & 0 & 0 \\ 0 & c_{23} & s_{23} \\ 0 & -s_{23} & c_{23} \end{bmatrix} \begin{bmatrix} c_{13} & 0 & s_{13}e^{-i\delta_{\text{CP}}} \\ 0 & 1 & 0 \\ -s_{13}e^{i\delta_{\text{CP}}} & 0 & c_{13} \end{bmatrix} \begin{bmatrix} c_{12} & s_{12} & 0 \\ -s_{12} & c_{12} & 0 \\ 0 & 0 & 1 \end{bmatrix}, \quad (1.9)$$

where $c_{ij} = \cos \theta_{ij}$, and $s_{ij} = \sin \theta_{ij}$. In plain text, the matrix explains how one neutrino flavour is composed of different parts with different masses, and in the same way, how one mass eigenstate is composed of different flavours. Neutrino oscillation arises because neutrinos travel as mass eigenstates with different masses, therefore, different speed, but one can only produce or detect neutrinos in flavour eigenstates. The change within their mass components between production and detection due to phase difference causes the change of flavour at detection. For example, as a specific electron neutrino propagates, possibility of detecting other types of neutrino will increase and decrease along the way, making the electron flavour content of the particle ‘‘oscillate,’’ hence the name of the phenomenon.

Coming back to the maths, the probability of a flavour change from α to β is

$$P_{\alpha \rightarrow \beta} \equiv P(\nu_\alpha \rightarrow \nu_\beta) = \left| \langle \nu_\beta | \nu(t) \rangle \right|^2, \quad (1.10)$$

where $|\nu(t=0)\rangle = |\nu_\alpha\rangle$. The mass eigenstate propagation can be written as

$$|\nu_j(t)\rangle = e^{-iE_j t} |\nu_j(0)\rangle \quad (1.11)$$

with E_j being the energy of the mass eigenstate j . Putting this into eq. (1.10) and adding neutrino mixing relations, eqs. (1.6) & (1.7), leads to

$$\begin{aligned} \langle \nu_\beta | \nu(t) \rangle &= \langle \nu_\beta | \sum_j U_{\alpha j}^* |\nu_j\rangle e^{-iE_j t} \\ &= \langle \nu_\beta | \sum_j U_{\alpha j}^* \sum_\beta U_{\beta j} |\nu_\beta\rangle e^{-iE_j t} \\ &= \sum_j U_{\alpha j}^* U_{\beta j} e^{-iE_j t}, \end{aligned} \quad (1.12)$$

$$\left| \langle \nu_\beta | \nu(t) \rangle \right|^2 = \sum_{j,k} U_{\alpha j}^* U_{\beta j} U_{\alpha k} U_{\beta k}^* e^{-i(E_j - E_k)t}. \quad (1.13)$$

Since the masses of neutrinos are extremely small, the energy can be approximated to be

$$E_j = \sqrt{p_j^2 + m_j^2} \simeq p_j + \frac{m_j^2}{2p_j} \approx E + \frac{m_j^2}{2E}, \quad (1.14)$$

where $p_j = |\vec{p}_j|$ is the value of three-momentum, and E is the energy of the wave packet.

As a result, the oscillation probability can be expressed in this way:

$$P_{\alpha \rightarrow \beta} = \sum_{j,k} U_{\alpha j}^* U_{\beta j} U_{\alpha k} U_{\beta k}^* e^{-i \frac{\Delta_{jk} m^2 L}{2E}}, \quad (1.15)$$

where $\Delta_{jk} m^2 \equiv m_j^2 - m_k^2$, and L , the distance travelled, replaces t in the ultrarelativistic case.

After some lengthy calculation, eq. (1.15) is equivalent to

$$\begin{aligned} P_{\alpha \rightarrow \beta} = & \delta_{\alpha\beta} - 4 \sum_{j>k} \Re_e \left\{ U_{\alpha j}^* U_{\beta j} U_{\alpha k} U_{\beta k}^* \right\} \sin^2 \left(\frac{\Delta_{jk} m^2 L}{4E} \right) \\ & \pm 2 \sum_{j>k} \Im_m \left\{ U_{\alpha j}^* U_{\beta j} U_{\alpha k} U_{\beta k}^* \right\} \sin \left(\frac{\Delta_{jk} m^2 L}{2E} \right). \end{aligned} \quad (1.16)$$

In this fashion, the equation is clearly divided into a CP-conserving part (second term on the right of eq. (1.16)) and a CP-violating part (third term). That means, if there really is no CP violation in the lepton sector, the third term would be zero. But if there is, this can be shown by comparing the oscillation probabilities of the same oscillation pattern between neutrinos and antineutrinos, which is clear in the equation above as the sign in front of the third term is for neutrino positive and for antineutrino negative.

1.2.1 MSW Effect

Coming back to the solar neutrino problem mentioned above, predictions from the neutrino oscillation has matched the detections, thereby confirming the theory, although not in all energy range of neutrinos detected. In order to explain this, one has to distinguish between the oscillation in vacuum and in dense matter.

The neutrino oscillation presented above takes place in vacuum where the travelling neutrinos barely interact with the surroundings. But as neutrinos are produced in the Sun's core and then have to travel out of the Sun, there are just so many obstacles that neutrinos might "trip over." This matter effect is referred to as *Mikheyev–Smirnov–Wolfenstein (MSW) effect* after the three physicists who proposed the theory [12]. It states that the abundance of electrons and the lack of muons and taus in matter effectively make the flavour components within the travelling mass eigenstate experience different "frictions," as only electron neutri-

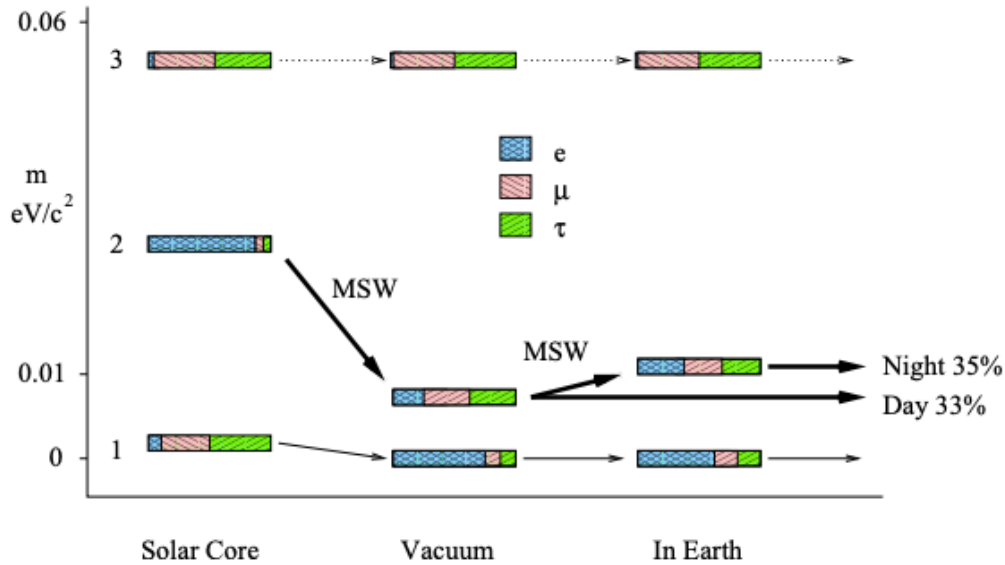


Figure 1.3 – Neutrino flavour components of the 3 mass eigenstates in the Sun, in vacuum and in Earth [12]

Note: m_1 in vacuum is assumed here to be zero, which may not be true in reality. The normal mass ordering ($m_3 > m_2$) is assumed. Also shown here is the detection deficit comparing to prediction without MSW effect, i.e. at day only 33% of electron neutrinos is detected, and at night 35%.

neutrinos can interact with electrons via CC interaction. The additional potential V the electron neutrinos experience can be reflected in the Hamiltonian: $H = H_0 + V$, where H_0 is the Hamiltonian in vacuum. This changes the mass eigenvalues corresponding to this Hamiltonian, so that neutrinos experience different effective masses when in matter. This effect is also observed when neutrinos travel through the Earth, making the measurement of solar neutrinos at night time (when they have to pass through the Earth to be detected) slightly different. This is illustrated in Figure 1.3. This effect is energy-dependent since it involves the interactions of neutrinos with matter. Therefore, the matter effect of low-energetic solar neutrinos is small and negligible, so that oscillation in vacuum would be already sufficient to predict the detection amount. On the other hand, it would be necessary to include MSW effect in the high-energy range if correct predictions are to be achieved.

1.2.2 Oscillation Parameters

PMNS matrix uses four parameters to describe the rotation between neutrino mass eigenbasis and flavour eigenbasis. There's also another pair of unknown parameters that come up in the oscillation probability equation (eq. (1.15)), i.e. the mass-squared differences

$\Delta_{21}m^2$ and $\Delta_{32}m^2$ (or $\Delta_{31}m^2$). Measuring these precisely is the goal of every neutrino oscillation experiment.

Since the detection of solar neutrinos may show higher precision in measuring the mixing of ν_e and ν_μ , the experiments conducting such a detection have measured the parameters θ_{12} and $\Delta_{21}m^2$, which are therefore called *solar parameters* θ_{sol} and Δm^2_{sol} . The current values were achieved also with the Kamioka Liquid Scintillator Antineutrino Detector (KamLAND) experiment [13]. Oscillation of the atmospheric neutrinos (neutrinos produced in the interaction of cosmic rays with the Earth’s atmosphere), on the other hand, exhibits more signatures of the mixing between ν_μ and ν_τ . For this reason, θ_{23} and $\Delta_{32}m^2$ (or $\Delta_{31}m^2$) are called *atmospheric parameters* θ_{atm} and Δm^2_{atm} . These were measured by the Super-Kamiokande detector together with some other long-baseline accelerator neutrino experiments like K2K (KEK to Kamioka) [14] and Main Injector Neutrino Oscillation Search (MINOS) [15]. Lastly, θ_{13} is with its smallness a difficult parameter to be measured precisely. However, measurements of the neutrinos produced in nuclear reactors may give the value of θ_{13} . Experiments like Daya Bay [16], Double Chooz [17] and Reactor Experiment for Neutrino Oscillation (RENO) [18] have all measured non-zero θ_{13} . This was also confirmed by long-baseline experiments T2K (Tokai to Kamioka) [19] and NuMI Off-Axis ν_e Appearance (NOvA) [20]. The 2018 best-fit values for all the parameters including δ_{CP} is presented in Table 1.2.

Table 1.2 – Best-fit oscillation parameters (bfp) with 1σ and 3σ uncertainties [21, 22]

Note: for the normal mass ordering, $\Delta_{3\ell}m^2 = \Delta_{31}m^2 > 0$; for the inverted mass ordering, $\Delta_{3\ell}m^2 = \Delta_{32}m^2 < 0$.

	Normal Ordering		Inverted Ordering	
	bfp $\pm 1\sigma$	3σ range	bfp $\pm 1\sigma$	3σ range
θ_{12} [°]	$33.82^{+0.78}_{-0.76}$	$31.61 \rightarrow 36.27$	$33.82^{+0.78}_{-0.76}$	$31.61 \rightarrow 36.27$
θ_{23} [°]	$49.6^{+1.0}_{-1.2}$	$40.3 \rightarrow 52.4$	$49.8^{+1.0}_{-1.1}$	$40.6 \rightarrow 52.5$
θ_{13} [°]	$8.61^{+0.13}_{-0.13}$	$8.22 \rightarrow 8.99$	$8.65^{+0.13}_{-0.13}$	$8.27 \rightarrow 9.03$
δ_{CP} [°]	215^{+40}_{-29}	$125 \rightarrow 392$	284^{+27}_{-29}	$196 \rightarrow 360$
$\Delta_{21}m^2$ [10^{-5} eV^2]	$7.39^{+0.21}_{-0.20}$	$6.79 \rightarrow 8.01$	$7.39^{+0.21}_{-0.20}$	$6.79 \rightarrow 8.01$
$\Delta_{3\ell}m^2$ [10^{-3} eV^2]	$+2.525^{+0.033}_{-0.032}$	$+2.427 \rightarrow +2.625$	$-2.512^{+0.034}_{-0.032}$	$-2.611 \rightarrow -2.412$

From the measurements, it is already worth noticing that one of the mass-squared differences is way larger than the other. Although the sign of $\Delta_{21}m^2$ can be determined by the solar neutrino measurements to be positive, there’s still uncertainty on the sign of the larger

mass-squared difference. Therefore, both mass orderings have to be considered: *normal* (mass) *ordering* (NO) when $m_1 < m_2 < m_3$ and *inverted* (mass) *ordering* (IO) when $m_3 < m_1 < m_2$, as shown in Figure 1.4. They may also be called “normal (mass) hierarchy (NH)” and “inverted (mass) hierarchy (IH)” in other literatures.

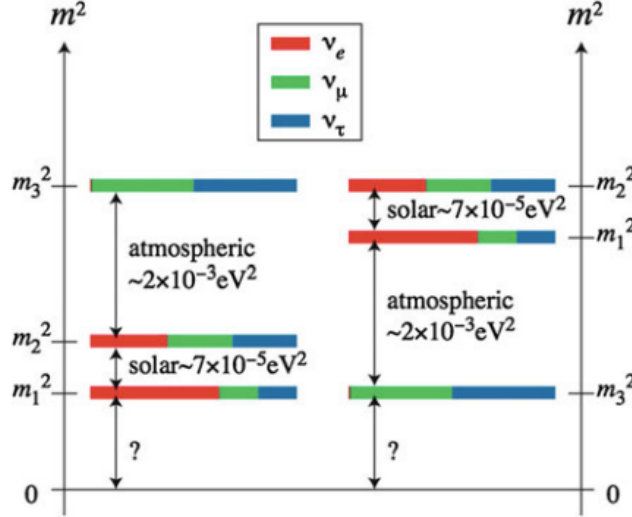


Figure 1.4 – Diagram of the possible mass orderings [1]

Left is NO; right is IO. The flavour components of each mass eigenstate are indicated by the corresponding colours. And the absolute neutrino masses are unknown.

1.3 Open Questions

Neutrino physics has come a long way to be what it is today, from Pauli’s attempt proposal to establishing theories around neutrinos. However, there are still some mysteries unsolved about this already mysterious particle even today. They will be introduced here in the following.

1.3.1 Precise Measurement of Oscillation Parameters

As presented in Subsection 1.2.2, there are still some uncertainties to the true values of the parameters. Current neutrino oscillation experiments including THEIA all aim to improve the precision in the parameters. Among all the parameters, there are three priorities: θ_{23} , δ_{CP} and the sign of $\Delta_{3l}m^2$ (i.e. the mass ordering).

The problem for θ_{23} is that it is very close to being maximal (expressed in the oscillation probability equation in the form of $\sin^2(2\theta_{23})$), that both values around 45° would be acceptable to the current precision measurements. This is the θ_{23} *octant degeneracy*. Although data

from the long-baseline experiments T2K and NOvA have shown preference on the second octant [21], this still has to be examined and confirmed by more experiments in the future.

As to measuring the CP-violating phase, results of the same oscillating pattern have to be compared between particle–antiparticle. That means, if $P(\nu_\alpha \rightarrow \nu_\beta) \neq P(\bar{\nu}_\alpha \rightarrow \bar{\nu}_\beta)$ with α and β representing flavours, $\delta \neq 0^\circ$ or 180° . Otherwise, neutrino oscillation would be CP-conserving. It wasn't clear what the CP phase should be until 2017–18, when combined experiment results have pushed the confidence interval of δ_{CP} towards 180° [21], and have preferred a mild CP violation in the case of NO and a close-to-maximal CP violation for IO. Again, further investigations have to be carried out to narrow down the uncertainty.

The mass ordering, as already shown above, is also undetermined. For that, long-baseline experiments with appropriate baseline length can be put into use to measure the sign. However, this posts an immense challenge as the precision measurement of the mass ordering has to take the precision of the two parameters mentioned above into consideration, and vice versa. Therefore, comparison of NO and IO with respect to other parameters has to be done each time to ensure better overall precision. Present global fit data from various long-baseline experiments and reactor experiments show a slight preference of NO over IO [21]. The inclusion of the atmospheric neutrino data from Super-Kamiokande further excludes the possibility of IO. The THEIA detector in a long-baseline experiment which will be introduced in Chapter 3 can also contribute to the determination of the CP phase and the mass ordering.

Another interesting topic on the oscillation parameters is the surprisingly large mixing angles. Comparing the PMNS matrix and its counterpart in the quark sector, the Cabibbo–Kobayashi–Maskawa (CKM) matrix, all three angles are small in the CKM matrix, whereas the solar mixing angle is about 34° and the atmospheric mixing is even almost maximal in the PMNS matrix. An interpretation would require more precision of the measurements, especially measuring the electron-flavour component in ν_3 . Should the parameters prove to have “special” meaning, it might just be an indication to physics beyond the Standard Model (BSM).

1.3.2 Neutrino Mass

Because of the introduction of neutrino oscillation, it is now certain that neutrinos have mass. Even though the mass-squared differences can be extracted from the oscillation data, it gives no clue on the absolute masses of neutrinos. Only a lower mass limit, $\sum m_{\nu_i} > 60 \text{ meV}$,

can be said from the differences. Therefore, other non-oscillation neutrino experiments have to be considered to determine the neutrino masses, e.g. from beta decay spectrum and the large-scale structure of the universe. Cosmological data from the Planck observatory in 2018 [23] give a constraint on the neutrino masses to be $\sum m_{\nu_i} < 0.12$ eV at 95% confidence level (CL). Direct measurement of the effective electron neutrino mass through studying the electron spectrum from beta decay of tritium is also possible. This was done by experiments in Mainz, Germany and Troitsk, Russia, where an upper limit of $m_{\nu_e} < 2.05$ eV at 95% CL was set [24]. The mass of electron neutrino presented here is of course a composition of the three mass eigenvalues:

$$m_{\nu_e}^2 = \sum |U_{ei}^2| m_i^2. \quad (1.17)$$

Following the same method, the Karlsruhe Tritium Neutrino Experiment (KATRIN) [25] would aim to measure the mass with a sensitivity of 0.2 eV. As of 2022, it has achieved an upper limit of $m_{\nu_e} < 0.8$ eV at 90% CL.

1.3.3 Majorana Neutrino

All the fermions discovered so far in the Standard Model fall under the category of *Dirac particles* (named after the physicist Paul Dirac), which means, they are essentially different from their antiparticles. The discussion of neutrinos above has also always treated them as Dirac particles. Ettore Majorana, on the other hand, proposed the idea [26] that an electrically neutral spin-1/2 particle can be identical to its antiparticle. Such particles would be termed *Majorana particles*. Neutrinos, as described in Subsection 1.1.1, exist only in left-chiral state as anti-neutrinos only in right-chiral state. In this sense, it is perfectly possible that neutrino and anti-neutrino are the same particle differentiated only by chirality. If this is true, it would be a fundamental change to the neutrino physics. For example, the PMNS matrix would have to be adjusted to consider two more phases α_1 and α_2 because of the redefinition of the fermionic fields. This is described by an additional matrix $\text{diag} \left(e^{i\alpha_1/2}, e^{i\alpha_2/2}, 1 \right)$, which will be multiplied to the original PMNS matrix from the right.

The search for the evidence has now begun. One way to do it is through searching for the *neutrinoless double beta* ($0\nu\beta\beta$) decay [27], which can only happen with the exchange of a virtual Majorana neutrino (Figure 1.5). In comparison, conventional double beta decay emits the Dirac neutrinos (or antineutrinos), which due to lepton number conservation cannot be reabsorbed in the process, and would appear in the final product. Experiments in search of $0\nu\beta\beta$

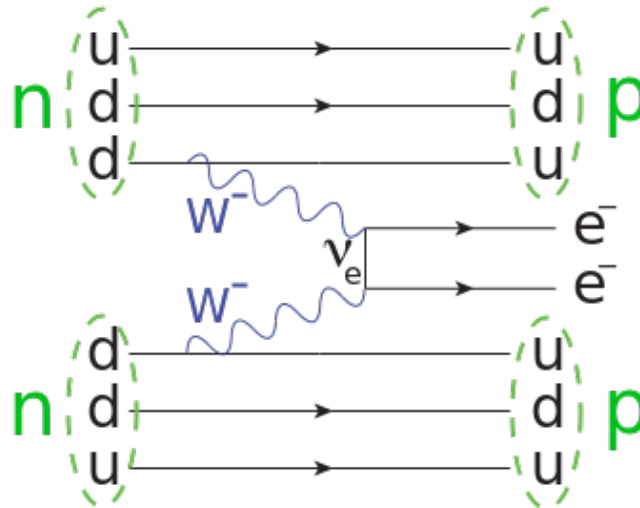


Figure 1.5 – Feynman diagram of $0\nu\beta\beta$ decay [28]

Two neutrons decay into two protons with by-products of two electrons. The absence of neutrinos in the final product suggests reabsorption between the two W vertices, which can only occur if neutrinos are Majorana particles.

decay are under way. However, no clear detection has been reported so far. Instead, the experiments were only able to set lower limits of the decay’s half-life. The Germanium Detector Array (GERDA) experiment, for example, published its result in 2020 [29] that the half-life is estimated to be $T_{1/2} > 1.8 \times 10^{26}$ years at 90% CL. In addition, a (Majorana) neutrino mass may be predicted from the half-life. Assuming that the decay is dominated by the exchange of light Majorana neutrinos, GERDA can set an upper limit of $m_{\beta\beta} < 79 - 180$ meV at 90% CL. This mass is the effective Majorana ν_e mass like the one in eq. (1.17) but with PMNS matrix fixed to include Majorana phases.

1.3.4 Sterile Neutrino

The fact that neutrinos always appear in left-chiral state and antineutrino always in right-chiral state has baffled the physics community for a long time, for this property is unusual considering other fundamental particles which can all exist in both chiralities. Thus, it seems unavoidable to ask: Do right-handed neutrinos and left-handed antineutrinos exist?

These hypothetical right-handed neutrinos (left-handed antineutrinos) are called *sterile neutrinos*, which are distinguished from the “active” left-handed neutrinos. The sterile neutrinos would not participate in weak interaction and, thus, interact only via gravity. This is to say that they will be very difficult to detect. However, evidence of their existence may be found in neutrino oscillation data. Several short-baseline experiments like MiniBooNE [30] have dis-

covered anomalies that can be explained by adding a new type or two of neutrinos to the existing three-neutrino PMNS matrix. This is supported by other reactor neutrino experiments [31], which also attributed the unexpected results to the possible existence of sterile neutrinos.

Currently, theories of sterile neutrino are still being developed. Their mass, although not known, is expected to be very large. The reason for this is that it can explain the extremely small masses of the known active neutrinos through the so-called seesaw mechanism in the Grand Unified Theory (GUT), where the mass of the active neutrinos is inversely proportional to that of the sterile neutrinos, $m_\nu \propto 1/M_M$. And since the particles don't carry any electric charge and only interact via gravity, they have become a natural candidate of dark matter [32], which is also a topic of great interest in modern-day cosmology.

Chapter 2

Neutrino Detection with THEIA

Detecting neutrinos is as mentioned in the previous chapter difficult, but not impossible. In this chapter, detection principles and techniques are presented before the introduction of the THEIA detector, which constitutes the main topic of this thesis.

2.1 Detection Principles

Since neutrinos don't carry any electric charge, they are not directly detectable. Instead, they can only be recognized by detecting the charged products from their interaction with a target. As described in Subsection [1.1.1](#), neutrino interaction can be divided into CC and NC interactions. In an NC interaction, neutrinos are detected by transferring some of their energy and momentum to a target. If the target is charged, like in

$$\nu_\ell + e^- \rightarrow \nu_\ell + e^-, \quad (2.1)$$

where $\ell = e, \mu, \tau$, the direction and/or the energy of the charged particles can then be measured to reconstruct that of the incident neutrinos. However, a flavour information of these neutrinos would not be available, as stated in eq. [\(2.1\)](#), in an NC interaction. A CC interaction, on the other hand, would involve the coupling of the neutrinos and their partner leptons, and therefore provide information on the neutrino's flavour, as in the reaction below for example:

$$\nu_\ell + e^- \rightarrow \ell^- + \nu_e. \quad (2.2)$$

For this reaction to occur, it would require that the incident neutrinos bear enough energy to create their partner leptons. This is especially true for ν_μ and ν_τ , since their partner leptons are heavier. The inverse beta decay in eq. [\(1.2\)](#) is essentially a CC interaction.

Neutrinos' interaction with matter happens very rarely due to the low cross sections. For neutrinos with $E_\nu \sim 10$ MeV for example, the cross section is about 10^{-40} to 10^{-44} cm² [[1](#)],

influenced by the neutrino flavour and the interaction type. Therefore, neutrino detectors are usually based on large volume of the target material to ensure the abundance of detected neutrinos. Furthermore, neutrino detectors are usually built underground to be shielded from the greatest source of background—cosmic rays, that are constantly bombarding the Earth.

2.2 Detection Techniques

In this section, a series of neutrino detection techniques relating to the THEIA detector will be introduced, as well as photo-detection techniques applied on neutrino detectors for the translation of detected events into analysable signals.

2.2.1 Scintillation

In the field of experimental physics, scintillators are a widely-used detection tool. The scintillation substance exhibits the property of *luminescence* upon contact with ionizing radiation (subatomic particles or electromagnetic waves with sufficient energy to ionize the material) [33]. It radiates light when particles pass through the scintillation material, thereby exciting the molecules along the way, which then re-emit the absorbed energy via photons. The relationship between the light yield L and the deposited energy E of the incident particles can be described by the Birks' law [34]:

$$\frac{dL}{dx} = S \frac{\frac{dE}{dx}}{1 + kB \frac{dE}{dx}}, \quad (2.3)$$

where S is the scintillation efficiency, and the so-called *Birks' coefficient* kB describes the quenching effect at regions of concentrated ionized molecules. The coefficient has units of distance per energy and must be determined for each type of material in use uniquely. If the quenching effect of a material is to be ignored, the light yield of this material would be as large as 10^4 photons per MeV of energy deposited [1].

The re-emission of the scintillation photons occur isotropically. Therefore, the directional information of the incident particles cannot be given. Furthermore, the relaxation process of the excited electron states may not be immediate. The actual photon emission time has to take into consideration the relaxation rate of different excited states in the scintillator. A probability density function (p.d.f.) $\Phi_{\text{em}}(t)$ of the photon emission time t with n decay components can be given as

$$\Phi_{\text{em}}(t; \tau, \omega) = \sum_{i=1}^n \frac{\omega_i}{\tau_i} e^{-\frac{t-t_0}{\tau_i}}, \quad (2.4)$$

where t_0 is the excitation time point and $t \geq t_0$. τ_i is the mean lifetime of decay component i and ω_i the component weight, which means the sum of all ω_i should be 1.

As described in Section [2.1](#), neutrino detection requires large volume of target. This is usually achieved using organic liquid scintillators (LSc), which are easier to be employed in a large amount and purified after use than the crystal scintillators. One example of LSc material is linear alkylbenzene (LAB)¹, which is a part of THEIA’s detector content. It is also common practice to add solutes such as 2,5-diphenyloxazole (PPO, C₁₅H₁₁NO) into the LSc solvent. These solutes serve as wavelength shifters that prevent the scintillation light to be absorbed while propagating inside the scintillator. Additionally, the shifted wavelength would match the region of efficiency of the surrounding photodetectors better.

According to the relation in eq. [\(2.3\)](#), the measured light yield gives an energy spectrum of the passing charged particles, which in turn can reconstruct the incident neutrino energy spectrum, enabling a calorimetric measurement of the neutrinos. In addition, the energy threshold for exciting an LSc molecule by charged particles is negligible in comparison with the energy required for the preceding neutrino interaction to occur. Therefore, the LSc detectors are considered the standard detection technique in measuring neutrinos in the energy range from few hundreds of keV to 100 MeV. For higher energy, the quenching effect would be substantial due to the large energy deposition according to the Birks’ law (eq. [\(2.3\)](#)), thereby undermining the efficiency of light production and limiting the calorimetric advantage of LSc. In this case, another type of detection technique is preferred.

2.2.2 Cherenkov Radiation

This detection technique that THEIA also utilizes depends on a physical phenomenon called *Cherenkov radiation*. As a charged particle passes through a dielectric medium with speed greater than that of light in that medium, “shockwaves” of Cherenkov radiation take place along the particle’s trajectory, similarly to the sonic booms [\[35\]](#). The shockwaves form a wavefront that propagates at a characteristic angle to the travelling direction of the particle. An illustration of the phenomenon is given in [Figure 2.1](#).

The Cherenkov angle θ_C in [Figure 2.1](#) can be calculated from the distances traversed by the light wavefront and the original particle in the same time period, i.e.

$$\cos \theta_C = \frac{1}{n\beta}, \quad (2.5)$$

¹ The chemical formula of LAB is C₆H₅CHR¹R², where R¹ = C_nH_{2n+1} and R² = C_mH_{2m+1}. m and n are integers, for which m ≥ 0, n ≥ 1, and the sum of both numbers lies typically between 9 and 15.

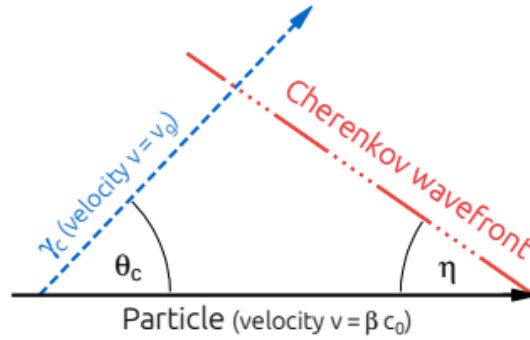


Figure 2.1 – Illustration of Cherenkov radiation [11]

Superluminal charged particles produce Cherenkov radiation that forms a wavefront (red) travelling in the direction of the blue dashed line with a group velocity $v = v_g$. In the case of no dispersion, v_g is the speed of light in the medium, and $\theta_c + \eta = 90^\circ$.

where n is the refraction index of the medium, and $\beta = \frac{v}{c_0}$ is the ratio of the particle's speed in the medium to the speed of light in vacuum. From the eq. (2.5), it is clear that when $\beta = 1/n$, the Cherenkov angle vanishes.² This sets a threshold on the particle's velocity that has to be exceeded for the production of Cherenkov radiation in a given medium. When the threshold velocity β_t is given, the particle-dependent kinetic energy threshold $E_{k,t}$ can also be calculated from the relation:

$$E_{k,t} = \left(\frac{1}{\sqrt{1 - \beta_t^2}} - 1 \right) m c^2, \quad (2.6)$$

where m is the rest mass of the particle in question, and $c = 1$ for the use of natural units. A list of the velocity and energy thresholds for different mediums is given in Table 2.1. Due to these thresholds, neutrinos must possess enough energy to be detectable at a Cherenkov detector, which is the reason that Cherenkov detectors are mainly responsible for the high energy range of neutrinos.

Different from scintillation light, Cherenkov radiation occurs almost immediately when superluminal particles pass through the medium. Besides, one advantage arises when using a transparent medium (e.g. water) as the detector body, namely, the unhindered propagation of Cherenkov photons to the surrounding photodetectors, which is vital for a successful acquirement of potential neutrino events.

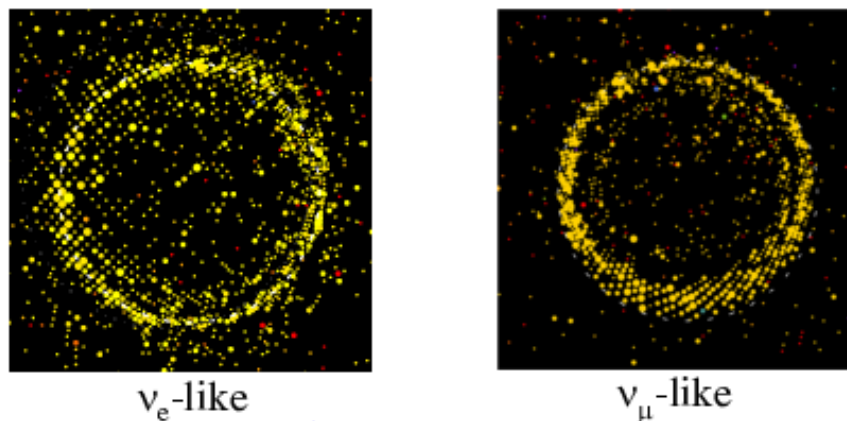
² This is somewhat self-explanatory, since at this threshold, the particle's speed meets the speed of light in that medium. In consequence, Cherenkov radiation doesn't occur.

Table 2.1 – Refraction indices and Cherenkov thresholds of different materials

Materials where the Cherenkov radiation can be observed are listed: ice (-7°C) [36], water (25°C) [37], LAB [38] and liquid argon (LAr) [39]. The shown refraction indices are measured with a wavelength of 430 nm.

	Material			
	Ice	Water	LAB (LSc)	LAr
Refraction index n	1.32	1.34	1.49	1.22
Threshold velocity β_t	0.759	0.747	0.671	0.820
Particle	Kinetic Energy Threshold [MeV]			
e^\pm	0.274	0.258	0.178	0.381
μ^\pm	56.7	53.4	36.9	78.8
π^\pm	74.9	70.5	48.7	104.1
K^\pm	265.0	249.4	172.3	368.1
p	503.6	474.0	327.4	699.7

Once the Cherenkov threshold is exceeded, shockwaves of Cherenkov radiation appear. The wavefront formed by the radiation propagates to the border of the detector, exhibiting a ring-like pattern at light detection (Figure 2.2). Unlike scintillation light, Cherenkov radiation could provide the directional information of the passing charged particles, and induce that of the incident neutrinos approximately. Additionally, an identification on the neutrino flavour may also be achieved by examining the property of detected Cherenkov rings (Figure 2.2).

**Figure 2.2** – Cherenkov rings of a ν_e -like event (left) and a ν_μ -like event (right) [40]

The points in the picture represent light detected by the photodetectors. Muons from ν_μ interactions travel almost straight through the detector, creating a sharp ring. Electrons, on the other hand, scatter easily because of their small mass, making the detected ring “fuzzier.”

2.2.3 Photo-Detection

After detecting the charged products from neutrino interaction via light signals, one needs to find a way to turn those light signals into electric ones for the subsequent analysis. This is realized by the application of *photodetectors* around the neutrino detector body. There are essentially several mechanisms with which photons can be translated into electric signals. However, for most neutrino detectors, photodetectors with photoelectric effect are the most popular. Below, two types of these photodetectors that will be implemented on THEIA detector are introduced.

Photomultiplier Tube

The first type is the *photomultiplier tube* (PMT). A simple structure of it is depicted in Figure 2.3. When a photon enters a PMT, an electron is emitted from the transmission photocathode via the photoelectric effect. This photoelectron (PE) then travels in the direction that is decided by the focusing electrode and hits the first dynode. At each dynode, more electrons will be knocked out by the previous electrons, and thus multiply themselves in this dynode chain. The multiplication factor depends on the number of dynodes and the potential difference applied between every two neighbouring dynodes. At the end of the cascade, the electrons are collected at the anode, resulting in a significant current pulse that can be measured easily. To avoid disturbance from gas molecules for example, the tube will be evacuated.

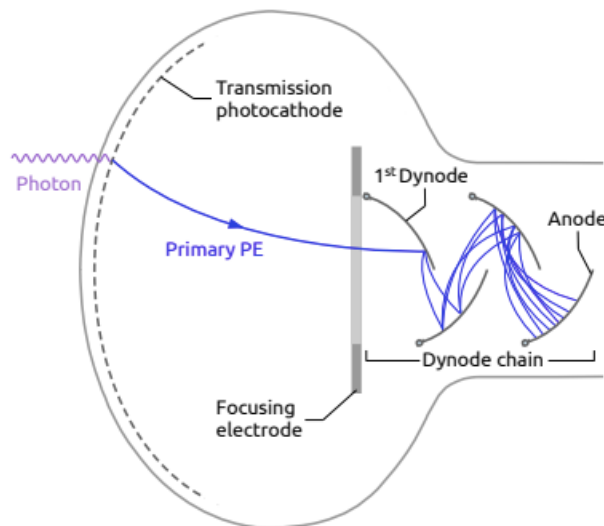


Figure 2.3 – Schematic of a photomultiplier tube [11]

The performance of the photocathode in a PMT can be manifested by the quantum efficiency (QE) of photon-to-electron conversion, $\eta(\lambda)$:

$$\eta(\lambda) = \frac{\text{number of photoelectrons released}}{\text{number of incident photons on cathode}(\lambda)}, \quad (2.7)$$

which depends on the wavelength (λ) of the incident photons and the material of the photocathode. Common materials listed in ref. [41] have variable QE ranging up to 27%.

The transit time between the emission of photoelectrons and the collection at the anode can be strongly influenced by the geometrical structure of the PMTs. Electrons created at the edge of the photocathode might need more time to hit the first dynode than the ones created in the middle. This problem can be counteracted easily by applying a spherical cathode like the one in Figure 2.3, so that the distance each electron has to travel would be equalized. However, the random energy and direction of the emitted electrons also have an effect on their transit time. The transit time spread (TTS), defined as the fluctuation of the transit time, is an indicator of the timing resolution of a PMT, i.e. the lower the TTS is, the better a PMT can resolve events at short time intervals. For most PMTs in use, TTS is in the range of 0.4 to 10 nanoseconds [41].

Large Area Picosecond Photo-Detector

The other type of photodetectors is the newly developed *Large Area Picosecond Photo-Detector* (LAPPD) [42]. The detection principle of an LAPPD is very similar to that of a PMT. The main difference of LAPPDs from the PMTs in their structures is the use of a set of *microchannel plates* (MCPs) instead of dynodes as the electron multipliers. An MCP is a plate which is composed of several tiny tubes (microchannels). Each channel functions as an independent electron multiplier, whose wall repeatedly creates secondary electrons when hit by the primary photoelectron or the multiplied electrons. In an LAPPD, two MCPs are stacked onto one another with small gap in between. The orientation of the two plates is arranged so that the microchannels would form a v-like shape. When electrons leave the MCPs, they travel to hit the read-out anode, which is, in this case, composed of thin strips. A detailed illustration of the LAPPD structure is presented in Figure 2.4.

The benefits of using MCP layers and anode strips are the LAPPD's ability to resolve photon events with small spatial distances of incidence, whereas the spatial resolution ability of a PMT is limited to the diametrical scale of the PMT (seen as a giant multiplication channel). According to recent development [42], LAPPDs have the capability of spatial resolution in the mm scale. As for the timing resolution, LAPPDs can also perform significantly better than the PMTs by limiting the electron transit time with thin plate layers (2 mm thick MCPs)

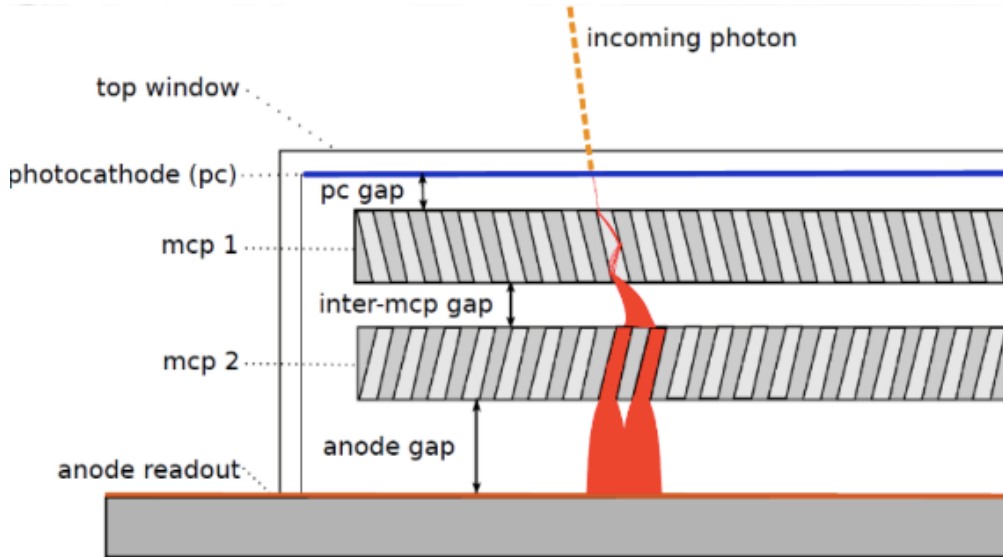


Figure 2.4 – Schematic of an LAPPD [43]

An incoming photon enters the LAPPD and hits the photocathode (up to 25% QE), creating a photoelectron, which is multiplied by the MCPs for read-out at the anode. The v-shaped angle of the channels serves to reduce ion feedback in the device, whereas the gap between the plates increases the signal gain. For the same reason as in PMTs, the device is evacuated.

and small distance from cathode to anode (about 1.5 cm). TTS of LAPPDs is about 50 ps, hence the name of the device.

2.3 THEIA Detector

Both scintillation and Cherenkov detectors have their advantages and their shortcomings. Scintillation detectors can provide a good energy resolution of the detected particles while not possessing an intrinsic energy threshold. However, the scintillation signals may not indicate any directional information of the incident neutrinos because of the isotropic nature of the signals. Cherenkov detectors, on the other hand, do reveal the travelling direction of neutrinos and can even recognize the flavour in question. Nevertheless, they do not respond to particles below the Cherenkov (energy) threshold.

With the goal to combine the advantages of these two detection techniques and counteract their shortcomings, a new type of detectors is being developed—THEIA, named after the Greek goddess of sight and vision [44]. Such a detector will reach greater performance in neutrino detection and may bring experimental neutrino physics to the next level with the help of novel target liquids and fast-timing photodetectors. The concept and the realization of this future neutrino detector will be introduced in the following.

2.3.1 Detector Concept

THEIA is designed to act simultaneously as a scintillation detector and a Cherenkov detector. In order to achieve this with large volume of target and cost-effectiveness, the content of THEIA has to be adjusted accordingly. In the recent development of the Advanced Scintillation Detector Concept (ASDC) [45], the *water-based liquid scintillator* (WbLS)—a mixture of water and liquid scintillator—has the ability to produce both scintillation and Cherenkov light upon incidence of high-energetic charged particles with an optimized ratio, and can ensure detection of particles below the Cherenkov threshold with scintillation light. Other benefits include good transparency to light signals, increase of overall light yield, and improvement of particle identification through comparison of scintillation to Cherenkov signals. This novel medium is typically constructed with 1–10% of LAB-based LSc mixed into water. The realization of this liquid in THEIA is currently in research and development (R&D) stage.

Now that the production of both scintillation and Cherenkov signals is assured, the separation of them is also important for the sake of the quality of detection. The possibility of this separation is largely due to the emission time difference between scintillation and Cherenkov photons, which is influenced by the composition of WbLS. Apart from that, the separation is made possible also by the newly available PMTs and ultrafast-timing LAPPDs. Besides, an employment of both types of photodetectors may improve the vertex and tracking resolution of photons, and therefore is considered by THEIA.

Since the last application on large water optical neutrino detectors, progress with PMT performance has been made. PMTs that possess higher than 35% QE photocathodes are now available from multiple suppliers. In addition, an improvement of the timing resolution (1.3 ns TTS) is observed [46]. As for the LAPPDs, further R&D is underway for their applicability on THEIA. A substantial improvement in vertex resolution can be achieved with LAPPDs, however, their performance in Cherenkov/scintillation separation may be overrated since light dispersion has a greater influence in the separation over the size of the detector [44]. The inclusion of LAPPDs is still planned in the realization of THEIA, but will not be assumed in the detector performance simulation (Subsection 3.1.3) to ensure not too optimistic results.

The above mentioned technologies are all under R&D for the application in THEIA. Among the several physics programmes THEIA has envisioned, this thesis focuses on the application in a long-baseline neutrino oscillation experiment. Therefore, only the corresponding detector configuration will be mentioned and introduced in the following subsection.

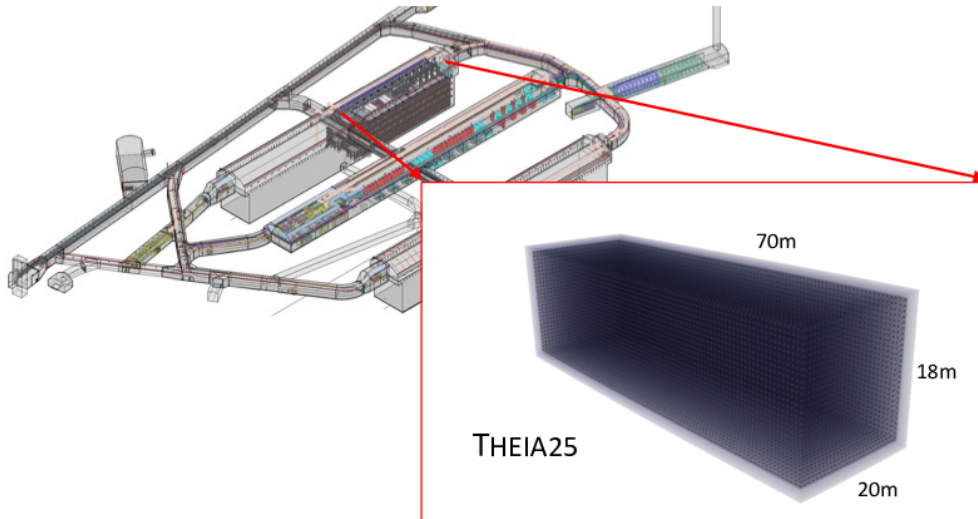


Figure 2.5 – Geometric scale and placement of THEIA-25 in one of the four LBNF caverns [44]

2.3.2 Realization in a Long-Baseline Experiment

For the realization, the detector is proposed to be built in a long-baseline neutrino oscillation experiment. The experiment is planned at the Long-Baseline Neutrino Facility (LBNF) [47] in the United States, which will be further introduced in Chapter 3. THEIA serves to detect the oscillated neutrinos at the far end (far site) of LBNF.

The detection of the oscillated neutrinos is conducted in the four LBNF underground caverns. Therefore, the design of the THEIA detector has to take into consideration the geometric scales of the caverns, where one THEIA configuration with a total detector body mass of 25 kt (THEIA-25) is to be employed accordingly. The detailed design and placement of this THEIA-25 are shown in Figure 2.5. The detector will be covered with uniformly distributed standard 10-inch PMTs (86%) and 20 cm \times 20 cm LAPPDs (4%) [44].

Another configuration of THEIA with a total detector mass of 100 kt (THEIA-100) is also in consideration for the fact that a better detector performance can be generally achieved with a larger detector body. The photodetector coverage percentage for THEIA-100 is the same as in the case for THEIA-25. THEIA-100, however, is designed regardless of the geometry of LBNF caverns, and therefore must be constructed elsewhere. Nevertheless, in this general detector performance study, both configurations will be considered in the following experiment simulation.

Chapter 3

Long-Baseline Neutrino Oscillation Experiment

As mentioned before, this thesis focuses only on THEIA’s application in a long-baseline neutrino oscillation (LBNO) experiment, whose goal is to measure the oscillation parameters to a higher level of precision, and to look for indication of CP violation and the correct mass ordering. The “baseline” where neutrino oscillation takes place is underground and stretches for hundreds of kilometres. For such an experiment, neutrinos produced at particle accelerators are used as the source for the reason of their stability and controllability. They can deliver high-energetic neutrinos of up to tens of GeV. At the other end of the baseline, a neutrino detector will be situated and detect the oscillated neutrinos. Additionally, another neutrino detector may be placed near the neutrino source for the purpose of beam monitoring.

THEIA’s application is proposed at the Long-Baseline Neutrino Facility (LBNF) [47] in the United States. At LBNF, two places are connected together: the Fermi National Accelerator

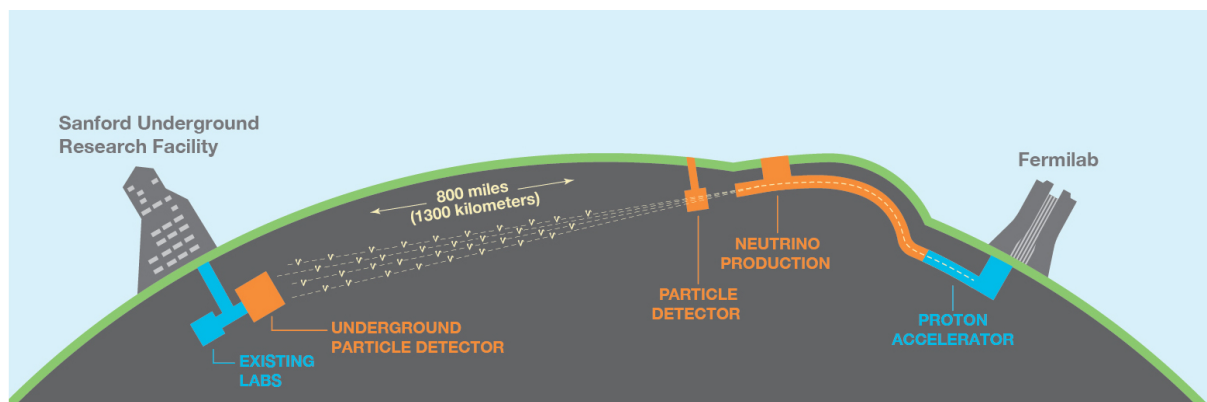


Figure 3.1 – Illustration of the Long-Baseline Neutrino Facility [49]

The colour orange represents the LBNF components to be constructed. The existing structures are marked blue. Two particle detector sites are shown: a near site situated downstream of the neutrino beam production and a far site underneath SURF.

tor Laboratory (Fermilab) in Illinois, where the neutrinos are produced, and the Sanford Underground Research Facility (SURF) in South Dakota, where the neutrinos are detected. The baseline between production and detection has a length of 1,300 km, longer than the currently existing similar experiments like T2K (295 km) or NOvA (810 km). Apart from THEIA, this facility also houses the Deep Underground Neutrino Experiment (DUNE) [48] as the main physics programme, which will provide neutrino detectors at the far site (DUNE-FD) and a beam monitoring complex at the near site (DUNE-ND). As for THEIA, its proposed site will be in one of the four caverns at the far site as mentioned in Subsection 2.3.2. An illustration of the facility is presented in Figure 3.1.

3.1 Experiment Description

A general neutrino oscillation experiment can be divided into three parts—production, oscillation (baseline) and detection. In the following subsections, each part will be described in detail in the environment of LBNE, and at the end, THEIA’s expected performance in the experiment will be discussed.

3.1.1 Neutrino Beam Production

In a long-baseline experiment, the stability and the intensity of the source neutrinos are essential to the success of the experiment. Particle accelerators, which produce neutrinos with energies up to tens of GeV in a controllable manner, are particularly suitable for such an

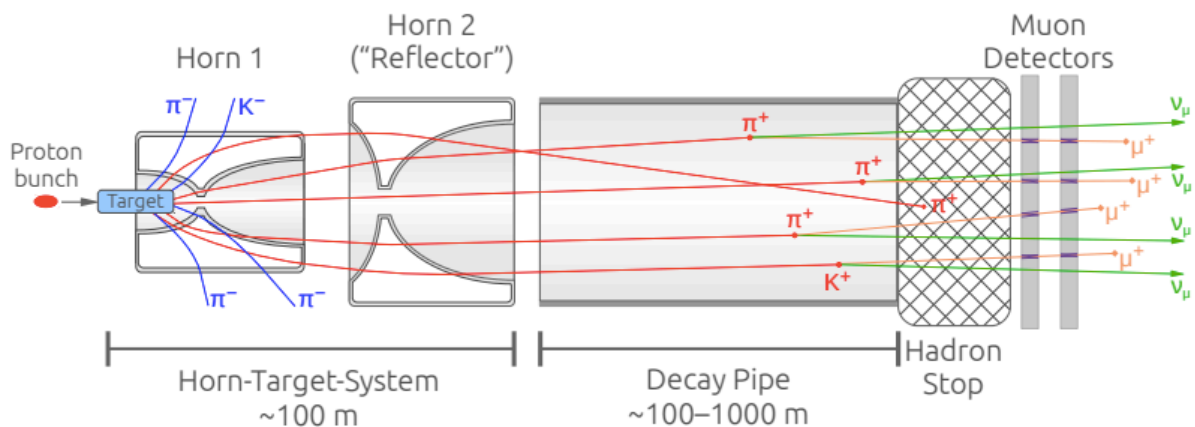


Figure 3.2 – Illustration of the production of neutrino beam from accelerators [11]

Depicted here is the production of ν_μ beam. An antineutrino production means only the reverse of magnetic fields in the focusing horns so that the negatively charged mesons are to be focused and positively charged ones deflected.

experiment. For the experiment at LBNF, neutrinos are produced at the Main Injector (MI) accelerator of Fermilab. In the following, the production principles of these *accelerator neutrinos* will be introduced.

To produce a neutrino beam, bunches of protons are accelerated to high energy in the accelerator and occasionally ejected out of the accelerator ring into an additional facility to collide with a stationary target. The collision with the target would produce all types of particles (mostly mesons like pions and kaons) that can be sorted by their electric charge and focused into a beam with a help of a series of magnetic horns. These secondary particles then enter the decay pipe where they decay into neutrinos or antineutrinos based on the selected charge of the mesons. The possible decay channels are listed below together with their branching ratios (BRs) [50]:

$$\pi^+ \rightarrow \mu^+ + \nu_\mu, \quad \pi^- \rightarrow \mu^- + \bar{\nu}_\mu, \quad \text{BR: } 99.99\%, \quad (3.1)$$

$$\pi^+ \rightarrow e^+ + \nu_e, \quad \pi^- \rightarrow e^- + \bar{\nu}_e, \quad \text{BR: } 0.01\%, \quad (3.2)$$

$$K^+ \rightarrow \mu^+ + \nu_\mu, \quad K^- \rightarrow \mu^- + \bar{\nu}_\mu, \quad \text{BR: } 63.56\%, \quad (3.3)$$

$$K^+ \rightarrow \mu^+ + \nu_\mu + \pi^0, \quad K^- \rightarrow \mu^- + \bar{\nu}_\mu + \pi^0, \quad \text{BR: } 3.35\%, \quad (3.4)$$

$$K^+ \rightarrow e^+ + \nu_e + \pi^0, \quad K^- \rightarrow e^- + \bar{\nu}_e + \pi^0, \quad \text{BR: } 5.07\%, \quad (3.5)$$

$$K_L^0 \rightarrow e^+ + \nu_e + \pi^-, \quad K_L^0 \rightarrow e^- + \bar{\nu}_e + \pi^+, \quad \text{BR: } 40.55\%, \quad (3.6)$$

$$K_L^0 \rightarrow \mu^+ + \nu_\mu + \pi^-, \quad K_L^0 \rightarrow \mu^- + \bar{\nu}_\mu + \pi^+, \quad \text{BR: } 27.04\%. \quad (3.7)$$

In order to produce a pure beam with one specific type of neutrinos, the length of the decay pipe must be adjusted for the optimization of pion decays and the suppression of the subsequent muon decays, which produce unwanted flavours and signs of neutrinos [51]:

$$\mu^+ \rightarrow e^+ + \bar{\nu}_\mu + \nu_e, \quad \mu^- \rightarrow e^- + \nu_\mu + \bar{\nu}_e, \quad \text{BR: } \approx 100\%. \quad (3.8)$$

Nevertheless, contaminations from $\nu_e/\bar{\nu}_e$ are still unavoidable, like shown in eqs. (3.5) & (3.6). Decays of muons and neutral kaons contribute to $\approx 1\%$ of $\nu_e/\bar{\nu}_e$ flux contamination [52]. Moreover, decays of unsuccessfully focused mesons may also contaminate the neutrino beam with the wrong sign, which would account for up to 10% of flux contamination.

The remaining mesons and the protons that leave the target without interaction are absorbed at the hadron stop by the far end of the decay pipe. When needed, a set of muon detectors can be placed after the hadron stop for the purpose of neutrino beam monitoring, which is available with the detection of the accompanying muons. The neutrinos, being relativistically boosted in the momentum direction of the focused mesons and the original protons, would travel from here onward without much disturbance.

Table 3.1 – Summary of the proton beam properties from LBNF [47]

Listed parameters are proton beam energy E_{beam} , number of protons per cycle, cycle time, beam power P_{beam} and number of protons-on-target (POT) per year. An operational uptime of 56% is assumed.

Parameter	Value		
E_{beam} [GeV]	60	80	120
Protons per cycle	7.5×10^{13}	7.5×10^{13}	7.5×10^{13}
Cycle time [s]	0.7	0.9	1.2
P_{beam} [MW]	1.03	1.07	1.2
POT / year [10^{21}]	1.89	1.47	1.10

The design of beamline facility at LBNF resembles the general illustration in Figure 3.2. The protons are accelerated in the upgraded version of MI according to the Proton Improvement Plan-II (PIP-II) until energies of 60 to 120 GeV, which correspond to a beam power of 1.03 to 1.2 MW. Afterwards, the proton bunch is extracted from MI and redirected towards the graphite target for the subsequent neutrino production. A technical overview of the proton beam properties is presented in Table 3.1, where an efficiency of LBNF (efficiency and uptime of accelerator and beamline) is assumed to be 56% [47].

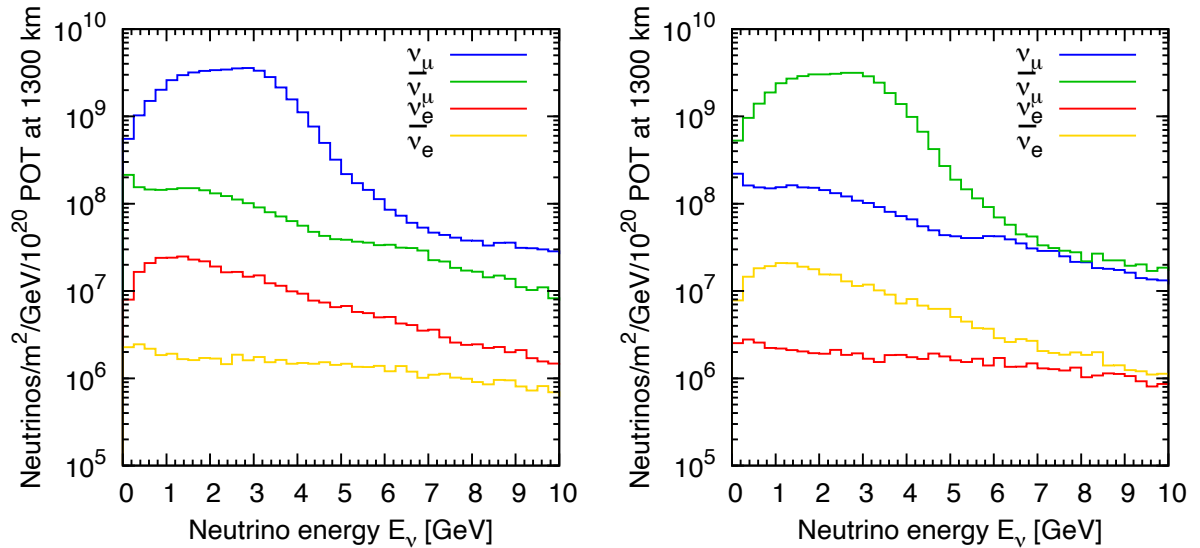


Figure 3.3 – Unoscillated neutrino and antineutrino flux spectra at 1,300 km from the beam source in FHC (left) and RHC (right) modes
The flux profile is provided by ref. [53].

According to the current direction in the magnetic horns, two operation modes are assigned: forward horn current (FHC) mode and reverse horn current (RHC) mode. FHC mode focuses the positively charged particles after protons have hit the target, thus producing mainly neutrinos. With just the reverse of current direction, RHC mode would produce mainly antineutrinos. However, as already explained in the production principles above, the production of the wrong-sign neutrinos is still unavoidable. Figure 3.3 shows the flux spectra in the absence of neutrino oscillation expected at 1,300 km from the beam source, where THEIA will be situated.

3.1.2 Baseline

After production, neutrinos travel and oscillate over 1,300 km underground, where the MSW effect plays a significant role in neutrino oscillation, and thus has to be considered in the simulation. However, a thorough investigation of matter density along the baseline is unrealistic and unachievable considering the depth of the baseline (30 km at the mid-point). Instead, a globally assumed mass density with an additionally imposed density uncertainty in the analysis is already capable of approximation of the real situation. For the experiment simulation in this thesis, the data from Preliminary Reference Earth Model (PREM) is taken [54, 55], which gives an average matter density of the crust to be 3.22 g/cm^3 , and a 1σ uncertainty on the number is assumed to be 2% for the whole baseline [53].

3.1.3 Detector Performance

Regardless of the practical execution, both configurations of THEIA will be discussed in this subsection. In order to discuss their performance, a fiducial cut has to be assumed with each configuration. This procedure serves to prevent downgraded performance due to background domination at regions close to the detector walls. Therefore, the fiducial mass is more physically significant than the total mass in the experiment. For the following experiment simulation, a similar cut is applied to both THEIA-25 and THEIA-100, which then have a fiducial mass of 17 kt and 70 kt respectively.

Since R&D of THEIA applied with WbLS and LAPPDs is still ongoing, the statement about the detector performance here can only be provisional. For the simulation presented later, the assumption that THEIA performs as well as a conventional pure water Cherenkov detector (WCD) is made [44], so that the simulation results would show a minimum ability of the detector. Improvements from the employment of WbLS and LAPPDs can then be includ-

ed in the future. The WCD model here is the Super-Kamiokande detector, whose neutrino interaction cross sections [56, 57] (Figure 3.4), event energy resolution function (introduced in the following) and event selection efficiencies (Subsection 3.2.1) are assumed for THEIA.

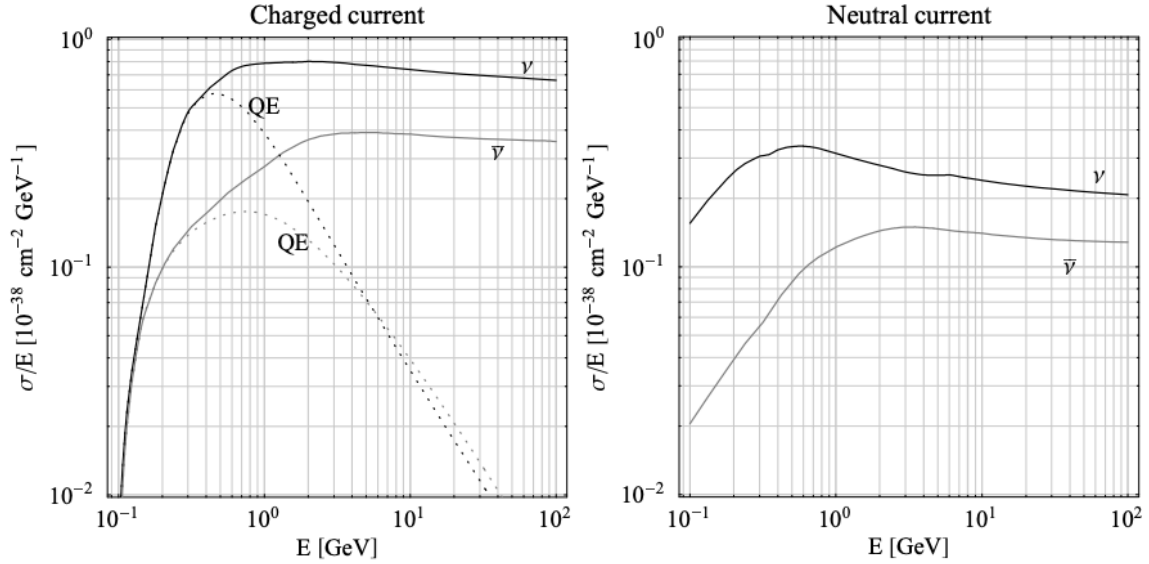


Figure 3.4 – Total neutrino (black curves) and antineutrino (grey curves) interaction cross sections σ divided by (anti-)neutrino energy E of charged current (left) and neutral current (right) as a function of E [58]

Additionally, the cross sections of charged-current quasi-elastic (QE) interactions, which dominate at energy around 1 GeV, are shown with dashed curves.

Since a WCD is only sensitive to charged leptons, a measurement of the hadronic energy deposition from neutrino interactions is not available. Therefore, the energy reconstruction is only achievable through studying the charged-current quasi-elastic (CCQE) interactions, which produce no other hadronic by-products. The CCQE interactions can be expressed as

$$\nu_\ell(\bar{\nu}_\ell) + N \rightarrow \ell^-(\ell^+) + N', N \neq N', \quad (3.9)$$

where N represents nucleons, and ℓ represents leptons. The inverse beta decay (eq. (1.2)) belongs to this category. Looking at eq. (3.9), one can assert that the energy transfer between leptons and nucleons during the interaction would be small due to the mass difference between them (i.e. quasi-elastic scattering). Thus, by simply detecting the leptons from CCQE interactions, the neutrinos' energy can then be reconstructed accordingly.

The energy resolution of this detector is shown in Figure 3.5. The inaccuracy of the reconstructed energy is largely due to the Fermi motion (quantum motion) of the nucleons. Since the Fermi motion is (neutrino-)energy-independent, the distribution in Figure 3.5 can be described by a Gaussian function with a constant width of 85 MeV in the analysis [58].

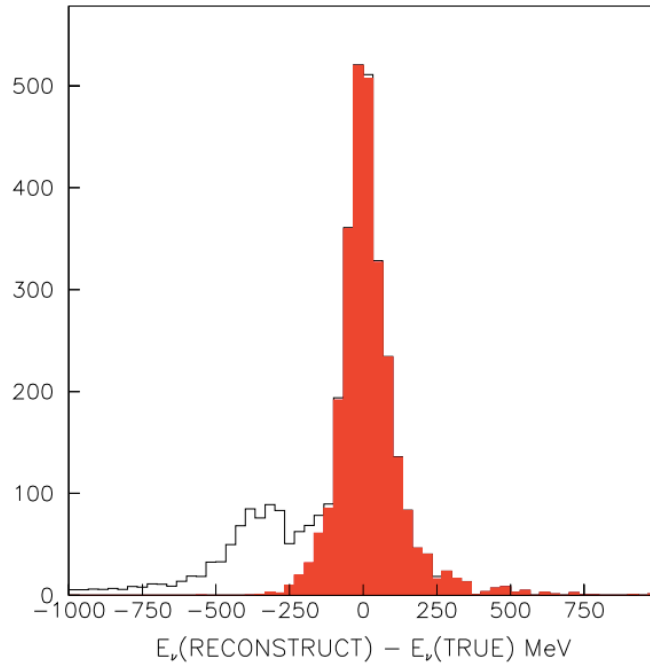


Figure 3.5 – Energy resolution of a water Cherenkov detector [59]

Energy resolution is represented by the difference between the reconstructed energy and the true incident energy of neutrinos. The red filled histogram represents CCQE events, while all CC events are represented in the open histogram.

3.2 Experiment Simulation

After acquiring the technical information of the experiment in the previous section, a simulation can be performed with the help of the *General Long Baseline Experiment Simulator* (GLOBES) software package [60, 61]. In order to obtain and understand the first-level results from the simulation, one remark has to be made regarding the computational algorithm of GLOBES. Unlike most simulation softwares, which use Monte Carlo (MC) method to simulate the stochastic nature of quantum interactions, GLOBES performs simulation without statistical fluctuations by utilizing the Asimov data set [62]. This is possible only by assuming that every set of input data (beam flux, cross sections, etc.) is presented as an average value over the fluctuations. Therefore, the simulation results are to be seen as the results of an “averaged” experiment.

To achieve the first-level results of oscillated neutrino event rates, a set of oscillation channels (specific oscillation patterns) will be chosen in the following. At the end, GLOBES will be able to process all the input (including that of the experiment environment described in the previous section) and produce the detected event rates expected from THEIA, which is then the starting point of the following sensitivity study.

3.2.1 Oscillation Channels

For the investigation of the true CP phase, the observation of the oscillation channel $\nu_\mu \rightarrow \nu_e$ ($\bar{\nu}_\mu \rightarrow \bar{\nu}_e$) is preferred, since the oscillation probability $P_{\mu \rightarrow e}$ ($P_{\bar{\mu} \rightarrow \bar{e}}$) varies the most with changing CP phases. To show this, one can examine the expression of the oscillation probability $P_{\mu \rightarrow e}$ including MSW effect [63]:

$$\begin{aligned}
 P_{\mu \rightarrow e} \simeq & \sin^2 \theta_{23} \sin^2 2\theta_{13} \frac{\sin^2(\Delta_{31} - aL)}{(\Delta_{31} - aL)^2} \Delta_{31}^2 \\
 & + \sin 2\theta_{23} \sin 2\theta_{13} \sin 2\theta_{12} \frac{\sin(\Delta_{31} - aL)}{(\Delta_{31} - aL)} \Delta_{31} \frac{\sin(aL)}{aL} \Delta_{21} \cos(\Delta_{31} + \delta_{\text{CP}}) \quad (3.10) \\
 & + \cos^2 \theta_{23} \sin^2 2\theta_{12} \frac{\sin^2(aL)}{(aL)^2} \Delta_{21}^2,
 \end{aligned}$$

where $\Delta_{ij} = \Delta_{ij} m^2 L / 4E_\nu$, $a = G_F N_e / \sqrt{2}$, G_F is the Fermi constant, N_e the number density of electrons in the Earth, L the length of the baseline, and E_ν the neutrino energy. $P_{\bar{\mu} \rightarrow \bar{e}}$ is expressed the same as in eq. (3.10) except with the signs of a (matter effect) and δ_{CP} (CP violation) switched. In addition to CP-asymmetry, the expression in eq. (3.10) introduces another neutrino-antineutrino asymmetry based on the matter effect, which can be simply explained by the lack of positrons in comparison to the abundant electrons existing in the Earth. Therefore, with increasing baseline length (i.e. neutrinos pass through more matter), the $\nu/\bar{\nu}$ asym-

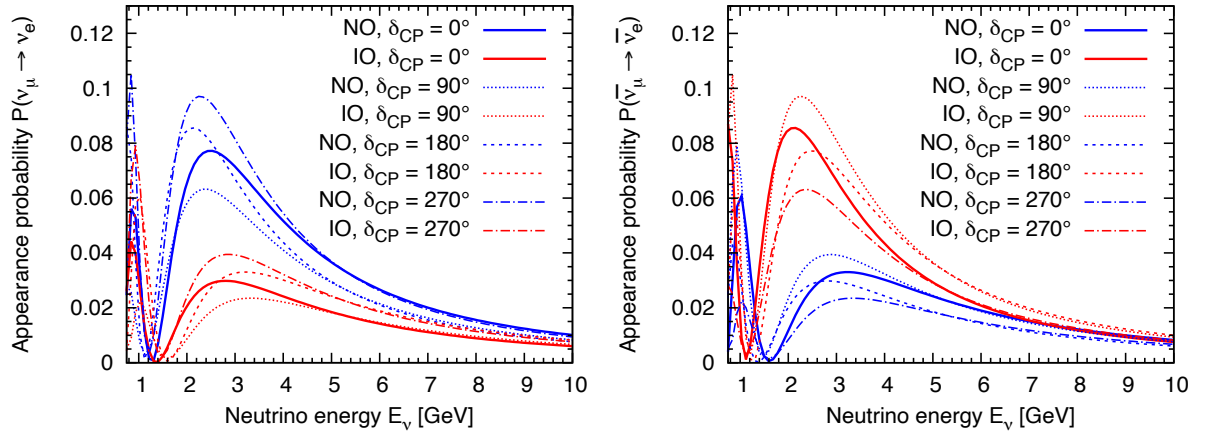


Figure 3.6 – Oscillation probabilities $P_{\mu \rightarrow e}$ (left) and $P_{\bar{\mu} \rightarrow \bar{e}}$ (right) at 1,300 km from beam source

The blue lines indicate true NO, and the red lines indicate true IO. Note that several values of δ_{CP} are shown, including $\delta_{\text{CP}} = 0^\circ$, 180° (CP conservation) and $\delta_{\text{CP}} = 90^\circ$, 270° (maximal CP violation). The oscillation parameters except δ_{CP} are the central values in Table 1.2.

metry becomes more significant. The expected $P_{\mu \rightarrow e}$ and $P_{\bar{\mu} \rightarrow \bar{e}}$ oscillation probabilities with a 1,300-km baseline are shown in Figure 3.6.

From Figure 3.6, the differences in oscillation probability are also clear between NO and IO in the lower neutrino energy range (few GeV). Thus, the determination of neutrino mass ordering can also be achieved by studying this oscillation channel. Since the neutrino source beam is comprised primarily of muon (anti-)neutrinos, this oscillation pattern is usually termed the name ν_e ($\bar{\nu}_e$) *appearance search*.

For this channel, the detector would have to look for $\nu_e/\bar{\nu}_e$ -like signatures by detecting their primary interaction products e^-/e^+ . However, as in every other scientific experiment, there are backgrounds that may appear in the detector. Since in long-baseline experiments, the intensity and the incident direction of the neutrino beam are well defined, backgrounds whose properties deviate from that of the beam neutrinos can be sufficiently rejected. Therefore, only beam-related backgrounds are considered in the simulation, i.e. not just one channel would exhibit $\nu_e/\bar{\nu}_e$ -like signatures. The considered backgrounds that contribute to the $\nu_e/\bar{\nu}_e$ appearance search are:

- intrinsic beam contamination ($\nu_e \rightarrow \nu_e, \bar{\nu}_e \rightarrow \bar{\nu}_e$),
- NC events that mimic $\nu_e/\bar{\nu}_e$ -like signatures (e.g. with π^0 production), and
- misidentified muons from $\nu_\mu/\bar{\nu}_\mu$ CC events.

The intrinsic beam contamination refers to detecting the unoscillated electron (anti-)neutrinos already contained in the beam. As for NC events, which do not reveal the neutrino flavour, it is possible that the products of NC interactions create electromagnetic showers which produce e-like Cherenkov rings.

Now that the possible backgrounds are listed, a set of event selection efficiencies has to be chosen for their composition in the simulation data. These selection efficiencies should represent the detector's ability to reject background events. However, a portion of the signal events (the desired events) may also be rejected during the background rejection process. This would then have to be reflected by the signal selection efficiency. For the $\nu_e/\bar{\nu}_e$ appearance search at THEIA, the selection efficiencies are listed in Table 3.2.

The selection efficiencies here are assumed to be global, i.e. independent of neutrino energies, and represent a conservative assumption for THEIA due to the measure taken in Subsection 3.1.3. Any further research effort regarding new technologies being applied on THEIA and/or improved event reconstruction techniques will be expected to improve the se-

Table 3.2 – Signal and background selection efficiencies of ν_e appearance search [59]

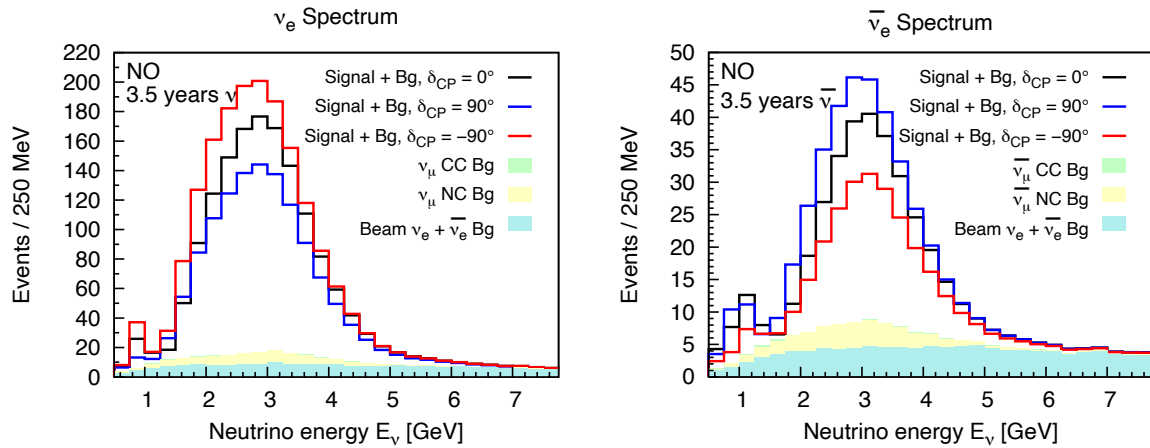
The oscillation product in NC events is stated as ν_x with $x = e, \mu, \tau$ due to the undetectability of flavour in NC interactions. For $\bar{\nu}_e$ appearance search, the same set of efficiencies is applied with the neutrino signs flipped in the oscillation channels. These numbers were also assumed for the T2K experiment.

Type		Oscillation & detection channel	Selection efficiency
Signal		$(\nu_\mu \rightarrow \nu_e)_{CC}$	0.505
Background	NC events	$(\nu_\mu \rightarrow \nu_x)_{NC}$	0.0056
	μ mis-ID	$(\nu_\mu \rightarrow \nu_\mu)_{CC}$	3.3×10^{-4}
	Beam contamination	$(\nu_e \rightarrow \nu_e)_{CC}$	0.505
		$(\bar{\nu}_e \rightarrow \bar{\nu}_e)_{CC}$	0.505

lection efficiencies from, for example, further reduction of NC events and muon misidentifications [44].

3.2.2 Simulated Event Rate

With the help of GLOBES, a first-level result of detected event rates can be extracted from the assumptions described above with the oscillation parameters (except δ_{CP}) from Table


Figure 3.7 – Expected event rates at THEIA-100 in 3.5-year FHC mode (left) and 3.5-year RHC mode (right)

Each energy bin has a width of 250 MeV. All signal and background (Bg) events of $\nu_e/\bar{\nu}_e$ appearance search are shown assuming NO is true. In addition, signals with different CP phases are displayed with different line colours ($\delta_{CP} = 0^\circ$ (black), 90° (blue), -90° (red)). The backgrounds are muon misidentification (sea green), NC events (lemon yellow) and beam contamination (turquoise).

1.2 (central values). A complete list of detected event counts is presented in Table 3.3. Consistent with DUNE, a beam exposure of seven years is assumed for THEIA, in which the operation time of FHC and RHC modes is equally distributed (i.e. 3.5 years each). Note that the annual operational uptime of the beam is 56%. Additionally, the energy spectra of the detected events at THEIA-100 are shown in Figure 3.7.

Table 3.3 – Expected event counts of $\nu_e/\bar{\nu}_e$ appearance search

All values are rounded to the nearest integers. The event counts are expected after the whole exposure time, i.e. 3.5 years for each mode, and are presented in the case of true NO and true IO (in parentheses). As expected, the detected events at THEIA-100 are roughly four times that at THEIA-25.

	THEIA-25		THEIA-100	
	FHC	RHC	FHC	RHC
$\nu_e/\bar{\nu}_e$ Signal				
$\delta_{\text{CP}} = 0^\circ$	316 (137)	63 (138)	1302 (566)	258 (567)
$\delta_{\text{CP}} = 90^\circ$	259 (105)	75 (160)	1065 (432)	310 (660)
$\delta_{\text{CP}} = -90^\circ$	379 (184)	43 (111)	1560 (758)	179 (458)
Beam $\nu_e + \bar{\nu}_e$ Bkg.	50 (52)	28 (27)	207 (214)	114 (112)
NC Bkg.	22 (22)	10 (10)	89 (89)	42 (42)
$\nu_\mu/\bar{\nu}_\mu$ CC Bkg.	1 (1)	0 (0)	4 (4)	2 (2)
Total Bkg.	73 (75)	38 (38)	300 (307)	158 (156)

In the following chapter, an analysis on these event rates is performed by examining the changes in the total rates and/or energy spectra from altering oscillation parameters, especially δ_{CP} , and assuming different mass orderings. With this method, a thorough study of the sensitivity of THEIA to leptonic CP violation and neutrino mass ordering can then be achieved.

Chapter 4

Simulation Data Analysis

With the help of GLoBES, future experiments like THEIA at LBNF can be simulated to demonstrate their potentials in solving the unanswered questions about neutrinos. In this thesis, the focus is on THEIA's sensitivity to detect leptonic CP violation and to determine the correct neutrino mass ordering. In order to obtain the desired information on this, an analysis of the simulated event rates in Subsection 3.2.2 is to be performed also using GLoBES software. The analysis procedure and the data evaluation are introduced in this chapter. At the end, results of these analyses will be presented as the final results of this thesis.

4.1 Analysis Procedure

Different from existing operating experiments, a future experiment doesn't have a real data reference, on which the analysis can be performed. Instead, it has to rely on the simulation data like the one in Subsection 3.2.2, for whose acquisition a specific set of oscillation parameters has to be chosen. These are assumed to be the *true parameter values* that are realized in nature. Compared to these, a set of *fit (test) parameter values* is chosen as an attempt to describe the expected experiment result based on true parameters. Therefore, the fit parameters may be altered accordingly to put different parameter assumptions to test. The goodness of fit between the predicted experiment results \mathbf{n}_{true} and the assumptions \mathbf{n}_{test} can be expressed in

$$\chi^2(\boldsymbol{\theta}_{\text{test}}) = -2 \ln L(\boldsymbol{\theta}_{\text{test}}), \quad (4.1)$$

where $\boldsymbol{\theta}_{\text{test}}$ represents the set of fit parameters, and L is the likelihood function of a specific assumption represented in $\boldsymbol{\theta}_{\text{test}}$. With the goal to find a better agreement between \mathbf{n}_{true} and \mathbf{n}_{test} , one has to look for a set of $\boldsymbol{\theta}_{\text{test}}$ that maximizes the likelihood function (i.e. greater probability of the assumption matching the actual data) and minimizes the χ^2 -function. Using this method, the assumption of any particular CP phase or any particular mass ordering can be

tested to show the detector’s response to these assumptions. In other words, the sensitivity of the detector can be revealed.

Before constructing the test statistics and defining the sensitivities for these assumptions, the issue of the systematic uncertainties of the experiment and the uncertainties of the oscillation parameters has to be addressed. In GLoBES analysis, the declaration of different uncertainties would allow the test data to change within these uncertainties. On one hand, it serves to further minimize the χ^2 -function to achieve a better agreement with the simulated results. On the other hand, it could prevent too optimistic results from different parameter assumptions that produce large χ^2 values. The treatment of uncertainties in the following is in accordance with the descriptions in the publication of THEIA [44].

4.1.1 Oscillation Parameter Uncertainties

For the minimization of the χ^2 -function, all oscillation parameters except δ_{CP} are allowed to shift within 1σ uncertainties. This is implemented by applying a set of external input as the errors of the true parameter values in the GLoBES analysis. As the true parameters and their uncertainties, the numbers from NuFIT 4.0 [21, 22] are adopted, and have been presented already in Table 1.2. For convenience, the same set of numbers and their input errors are listed again in Table 4.1. As for δ_{CP} , its value in the simulation does not consider any preference from prior experiment results, and therefore remains unknown. A scan of the whole range of

Table 4.1 – Oscillation parameter central values and 1σ errors in GLoBES analysis [21, 22]

Other than δ_{CP} , every value is based on the results from NuFIT 4.0. Since the probability distributions of these parameters are not all Gaussian, the 1σ error is constructed as $1/6$ of the $\pm 3\sigma$ range rather than $\pm 1\sigma$ shown in Table 1.2. This is especially true for θ_{23} . For the reason that GLoBES does not differentiate between $\Delta_{31}m^2$ in NO and $\Delta_{32}m^2$ in IO, the mass-squared difference is consistently given as $\Delta_{31}m^2$.

Parameter	Central value	Absolute error	Relative error
θ_{12} [°]	33.82	± 0.78	$\pm 2.3\%$
θ_{23} [°]	49.6	± 2.02	$\pm 4.1\%$
θ_{13} [°]	8.61	± 0.13	$\pm 1.5\%$
$\Delta_{21}m^2$ [10^{-5} eV ²]	7.39	± 0.20	$\pm 2.8\%$
$\Delta_{31}m^2$ [10^{-3} eV ²] (NO)	2.525	± 0.033	$\pm 1.3\%$
$\Delta_{31}m^2$ [10^{-3} eV ²] (IO)	-2.512	± 0.033	$\pm 1.3\%$

δ_{CP} is consequently necessary during the analysis, as the possible true value has to be in the interval $[0^\circ, 360^\circ]$.

4.1.2 Systematic Uncertainties

Other than oscillation parameter uncertainties, the uncertainties of the experiment itself are expressed by declaring the systematic uncertainties. These include the possible errors in the neutrino beam flux, the interaction cross sections, the energy reconstruction, etc. Recall that these experiment informations are treated as average values (Asimov data set, see Section 3.2) in GLoBES and no information on their uncertainties is given in the input file. Therefore, these uncertainties have to be represented in the overall systematic uncertainties.

The implementation of systematic uncertainties means that the detected (signal) event rate s_i^0 in the i th reconstructed energy bin can be renormalized in the fashion of

$$s_i = s_i^0 \cdot (1 + n_s), \quad (4.2)$$

where n_s is the (signal) *normalization parameter* constrained by the assumed (signal) uncertainty σ_{n_s} . The same statement applies to the background event rates b_i with background uncertainty σ_{n_b} , which is not necessarily identical to σ_{n_s} . During the process of χ^2 -minimization, the signal and background normalization parameters are subject to shift around zero, bounded by σ_{n_s} and σ_{n_b} respectively.

In the THEIA experiment, the signal and background uncertainties are assumed to be 2% and 5% respectively for the $\nu_e/\bar{\nu}_e$ appearance search [44]. This assumption takes into consideration the samples from $\nu_\mu/\bar{\nu}_\mu$ disappearance search (the oscillation channels $\nu_\mu \rightarrow \nu_\mu$, $\bar{\nu}_\mu \rightarrow \bar{\nu}_\mu$) which acts as a constraint for the parameter fitting in other simulations. That is to say, the inclusion of these channels in the simulation of this thesis is replaced by the decrease of the uncertainties for the appearance samples.

A further remark about the reduction of systematic uncertainties can be made with regard to the DUNE near detector complex (DUNE-ND) [64]. The purpose of DUNE-ND is to constrain the systematic uncertainties by monitoring the neutrino beam before oscillation and studying the neutrino interactions, with its detectors situated just downstream of the beam production facility. From the results of the DUNE-ND Fast Monte Carlo simulation [65], a 2.5% uncertainty on the absolute beam flux and a 1% to 2% uncertainty on the flux shape are predicted. Effort of studying the connection between DUNE-ND and THEIA on

the matter of cross section uncertainty reduction is also underway [44]. From this aspect, the assumption of 2% signal systematic uncertainty in this analysis is then justified [48].

4.1.3 Hypothesis Testing

In a sensitivity study, the ability of the detector to retrieve results deviating from a particular hypothesis in a theory is put to test. For this purpose, two competing, mutually exclusive hypotheses are ordered—a *null hypothesis* H_0 , the hypothesis that is the starting point of the test, and an *alternative hypothesis* H_1 , the hypothesis that suggests otherwise. The goal of hypothesis testing is to determine to what extent a particular hypothesis can be accepted or rejected based on the experiment statistics. In the following, a set of test statistics that measures the individual tests and eventually sets a criterion in the determination is constructed.

Test for CP Conservation

For the test of sensitivity to CP violation (CPV), H_0 is the hypothesis for CP violation, and H_1 is the hypothesis for CP conservation. The test statistics is expressed using χ^2 -functions as

$$\Delta\chi_{\text{CPV}}^2 = \min \chi^2 (\delta_{\text{CP}}^{\text{test}} = 0^\circ, 180^\circ) - \chi^2 (\delta_{\text{CP}}^{\text{true}} = [0^\circ, 360^\circ]), \quad (4.3)$$

where $\delta_{\text{CP}}^{\text{true}}$ is the CP phase assumed in the true parameter set $\boldsymbol{\theta}_{\text{true}}$, and $\delta_{\text{CP}}^{\text{test}}$ is the one assumed in the test parameter set $\boldsymbol{\theta}_{\text{test}}$. The objective of this test statistics is to show the deviations in test data from the assumption of CP conservation when the true CP phase might not be 0° or 180° . For this reason, this test is better to be called a *test for CP conservation*.

The eq. (4.3) restates the fact that the true CP phase is unknown. Therefore, $\Delta\chi_{\text{CPV}}^2$ has to be calculated with every value on the $\delta_{\text{CP}}^{\text{true}}$ axis. A minimization of $\chi^2 (\delta_{\text{CP}}^{\text{test}})$ between the test values 0° and 180° has to be performed additionally since both values indicate CP conservation. Contradict to a real experiment, where the predicted event spectra may not coincide with the spectra from the experiment results, these two spectra are identical in a simulated experiment, especially because GLoBES simulation does not apply statistical fluctuations. Therefore, $\chi^2 (\delta_{\text{CP}}^{\text{true}})$, which represents a comparison between the simulated data and the predicted data both with the same set of (true) parameters, is essentially zero.

In a general experiment, $\Delta\chi^2$ values are calculated with each experiment result repeatedly and collected afterwards. The distribution of this collection of $\Delta\chi^2$ would follow a Gaussian distribution with a mean value of $\overline{\Delta\chi^2}$ and a standard deviation of $\sqrt{|\overline{\Delta\chi^2}|}$ [48].

However, since the experiment results presented by GLoBES simulation are already assumed to be averaged, the test statistics based on these results would also be an average value of itself. Thus, the standard deviation σ is just the square root of the test statistics $\sqrt{\Delta\chi^2}$. Finally, the sensitivity corresponding to this test, characterized by the standard deviation σ , sets a criterion that bounds the confidence interval of the statement, that the null hypothesis is accepted (or that the alternative hypothesis is rejected). The sensitivity to CP violation could therefore indicate the confidence level of an experiment to accept CP violation hypothesis (or to reject CP conservation hypothesis) at a certain true parameter ($\delta_{\text{CP}}^{\text{true}}$). In Section 4.2, the sensitivity of THEIA to leptonic CP violation will be presented.

Tests for Mass Orderings

As for the test of sensitivity to neutrino mass ordering (MO), there are two scenarios that have to be considered. If NO is true, NO will be the null hypothesis H_0 in this case, and IO is the alternative hypothesis H_1 . The corresponding test statistics is

$$\Delta\chi_{\text{MO}}^2 = \chi_{\text{IO}}^2 - \chi_{\text{NO}}^2, \quad (4.4)$$

where the subscripts indicate adapting the test parameters θ_{test} to the corresponding case. With the same reasoning in the test for CP conservation, this test is called a *test for IO*. On the other hand, if IO is true, then $H_0 = H_{\text{IO}}$, and $H_1 = H_{\text{NO}}$. The test statistics is then

$$\Delta\chi_{\text{MO}}^2 = \chi_{\text{NO}}^2 - \chi_{\text{IO}}^2. \quad (4.5)$$

This is a *test for NO*. By the same argument as above, the second terms in eqs. (4.4) & (4.5) give zero in a simulated experiment.

The distribution of $\Delta\chi_{\text{MO}}^2$, however, follows a different Gaussian distribution function with mean value $\overline{\Delta\chi_{\text{MO}}^2}$ and standard deviation $2\sqrt{|\overline{\Delta\chi_{\text{MO}}^2}|}$. This fundamental difference is based on the fact that there exist only two distinctive parameter sets that represent NO and IO, while the whole parameter space of δ_{CP} is subject to the test. Therefore, the statistical meaning of the test statistics for mass orderings in terms of confidence levels requires special attention [66, 67]. An explanation of the statistics will be given after the sensitivity of THEIA to neutrino mass ordering is presented in Section 4.3, where the sensitivity is characterized by the square root of the test statistics $\sqrt{\Delta\chi_{\text{MO}}^2}$.

4.2 Result: Sensitivity to Leptonic CP Violation

In this section, the THEIA detector, which has a detector performance equivalent to that of a WCD in this analysis, in a long-baseline experiment at LBNF is tested for its sensitivity to detect leptonic CP violation using the aforementioned analysis procedure. The results are presented in Figure 4.1.

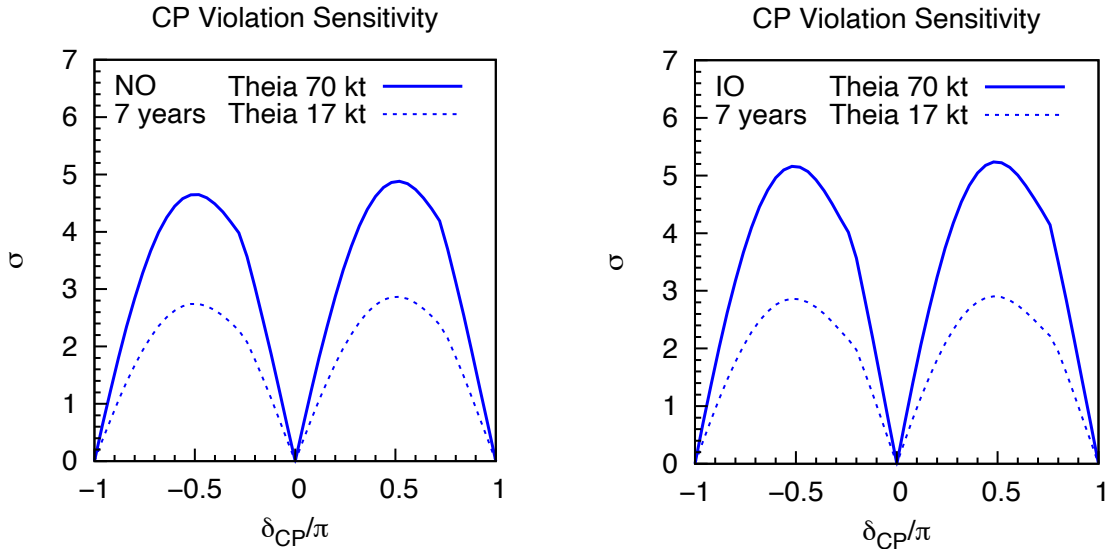


Figure 4.1 – THEIA’s sensitivity to CP violation in the cases of true NO (left) and true IO (right)

The x-axis indicates the true CP phases. The y-axis is the sensitivity expressed in standard deviations σ . Both configurations are considered—THEIA-25 (17-kt fiducial mass, dashed line) and THEIA-100 (70-kt fiducial mass, solid line). 7 years of beam exposure are assumed with equal operation time in FHC and RHC modes. The sensitivity drops to zero at two CP-conserving phases ($\delta_{\text{CP}} = 0^\circ, 180^\circ$) by definition.

Figure 4.1 exhibits the signature of peaks between the CP-conserving phases, at which the sensitivity is zero because there is no CP violation. By comparison of the two cases in Figure 4.1, a slightly higher sensitivity with true IO is observed. This can be explained by observing the total $\nu_e/\bar{\nu}_e$ signal event counts for different MO cases. According to the simulation results presented in Table 3.3, the event count has a clear excess of $\bar{\nu}_e$ events when $\delta_{\text{CP}} = 90^\circ$ and of ν_e events when $\delta_{\text{CP}} = -90^\circ$ in the case of true IO, which is beneficial to the examination of the different oscillation behaviour between neutrinos and antineutrinos (i.e. CP violation). Therefore, the detector is more sensitive to CP violation with true IO. On the other hand, while an increase of event counts can be observed in the same pattern with the case of true NO, there is still an overall excess of ν_e events over $\bar{\nu}_e$ events regardless of the CP phase.

This excess is mainly a result of the bigger interaction cross sections for neutrinos than anti-neutrinos.¹ Thus, in the case of true NO, the detector would be slightly less sensitive to CP violation due to this excess.

As for the statistical implication of sensitivity, the confidence intervals of a Gaussian distribution are assumed. For instance, a 1σ sensitivity means that CP violation hypothesis can be accepted (i.e. CP violation can be identified) at a CL of 68.27%. 2σ and 3σ sensitivity would in turn mean 95.45% and 99.73% CL respectively. In the field of particle physics, a result is considered to be an evidence of the phenomenon in question only with a statistical significance higher than 3σ . A discovery can only be asserted with a significance higher than 5σ (99.99994% CL). This convention comes from the need in particle physics to reduce the chance of incorrect statements about the results because of possible unknown systematic errors in the experiment.

By this convention, THEIA-100 is able to provide evidence of CP violation for 60% of the δ_{CP} parameter space, and even achieve a discovery in the case of true IO if the true CP phase is in the vicinity of 90° or 270° (maximally CP-violated). THEIA-25, on the other hand, has a peak sensitivity of 2.8σ with true NO and 2.9σ with true IO, which is approximately equivalent to the performance of a 10-kt (fiducial) DUNE-FD (17.1-kt total mass [47]) [44].

In general, a higher sensitivity can be achieved by extending the overall exposure of the detector to the beam. One method is to increase the detector volume that is exposed to the beam, as suggested by the increased sensitivity of THEIA-100 compared to THEIA-25. Otherwise, one can accomplish this by increasing the beam power or prolonging the exposure. The performance of THEIA under variable beam exposure can be seen in Figure 4.2, which shows the minimum sensitivity that can be achieved for 25%, 50% and 75% of δ_{CP} parameter space as a function of exposure. The unit for quantifying the exposure here is (detector fiducial mass \times beam power \times exposure duration) kt·MW·year.

A THEIA-100 with a standard 1.07-MW 80-GeV beam, taking data for seven years, corresponds to an exposure of 524.3 kt·MW·year. The exposure would be 127.33 kt·MW·year for the case of THEIA-25 with other conditions unchanged. As an example reference that can be extracted from Figure 4.2, a minimum exposure of 1415 kt·MW·year is necessary for achieving 5σ sensitivity for 50% of the parameter space. This corresponds to 19 years of data for THEIA-100 or 78 years of data for THEIA-25.

¹ With the same argument, the $\bar{\nu}_e$ events are largely reduced in the case of true IO as the result of the smaller cross sections. However, this turns out to be advantageous as it creates a balance between ν_e events and $\bar{\nu}_e$ events, that further increases the sensitivity.

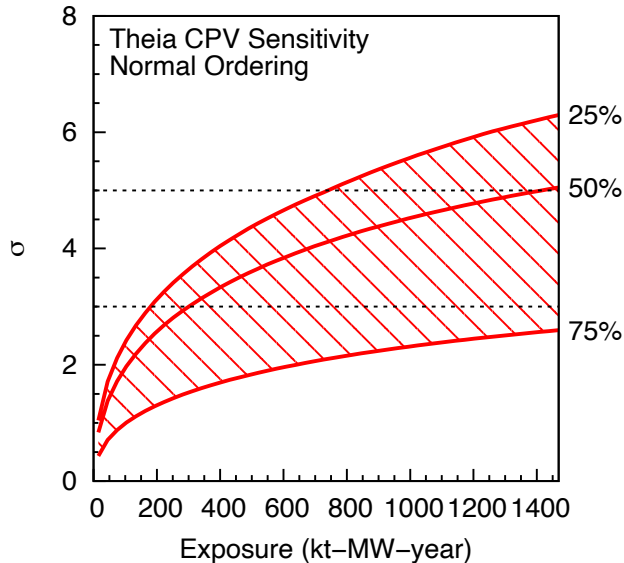


Figure 4.2 – Minimum sensitivity of THEIA to CP violation for 25%, 50% and 75% of δ_{CP} parameter space as a function of exposure (in $\text{kt}\cdot\text{MW}\cdot\text{year}$)

Assumed here is NO. Since the sensitivity in the case of true IO is higher than in the case of true NO, this plot may also be interpreted as the actual minimum sensitivity regardless of the true mass ordering.

While altering the detector volume may be subject to the limitation of space at the far site of LBNF, and tens of years of data taking may be somewhat unrealistic, such a high exposure requirement can be made possible with increased beam power, which is already envisioned in the future upgrade of MI accelerator [47]. The 2.4-MW beam from PIP-II upgrade could therefore help THEIA achieve the desired sensitivity to CP violation with the needed exposure time reduced.

4.2.1 Effect of Different Oscillation Parameter Assumptions

The impact of uncertainties in oscillation parameters on THEIA’s sensitivity can be seen from varying the true parameters assumed in the analysis. In the following, the variation in sensitivity to CP violation due to various true values of θ_{23} and θ_{13} is presented in Figure 4.3, and due to various true $\Delta_{31}m^2$ in Figure 4.4. The shown parameter range is the $\pm 3\sigma$ range around the central values in Table 1.2. During GLoBES minimization, the relative parameter error in the analysis, however, has to stay unchanged for preventing the minimizer to run into a wrong χ^2 minimum.

As seen from Figure 4.3, the uncertainty of θ_{23} has a significant impact on the sensitivity, which can be explained by the sizeable variation of $\sin^2\theta_{23}$ in eq. (3.10) that influences the outcome of the $\nu_e/\bar{\nu}_e$ appearance search significantly. The biggest sensitivity difference due to

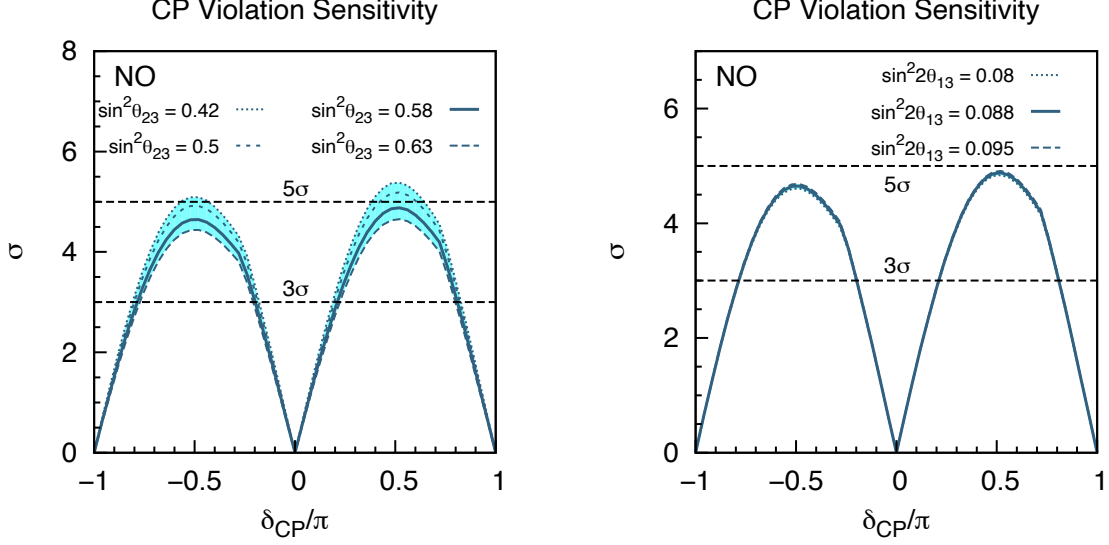


Figure 4.3 – Variation of sensitivity of THEIA-100 to CP violation due to different θ_{23} (left) and θ_{13} (right) true values

Both plots assume true NO and 7 years of beam exposure. The shaded area represents the $\pm 3\sigma$ uncertainty in the parameters in question, which have central values denoted by solid lines. In addition, the maximal θ_{23} is shown ($\sin^2\theta_{23} = 0.5$). For all values of δ_{CP} , the sensitivity increases as θ_{23} decreases and θ_{13} increases.

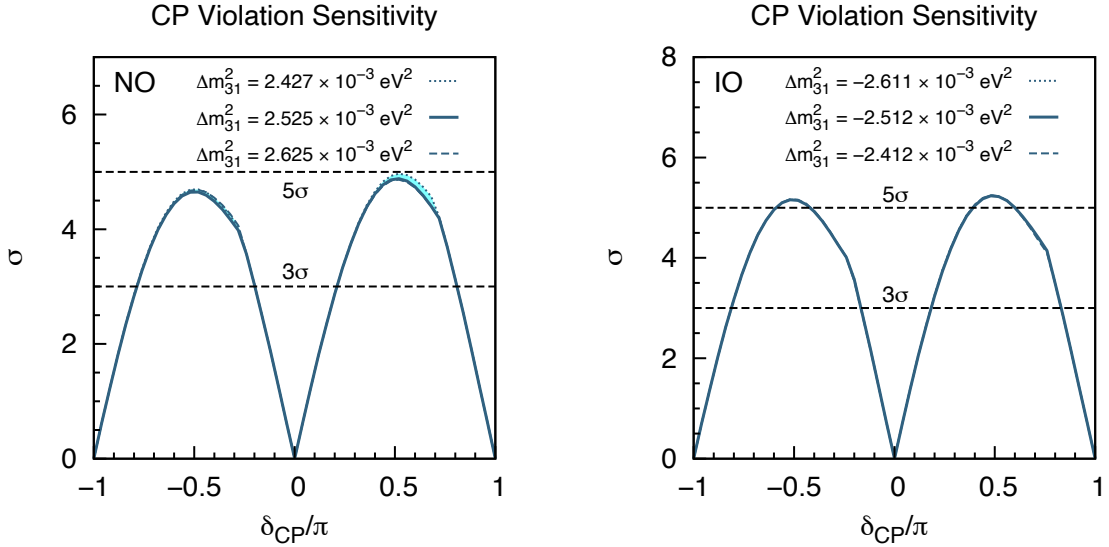


Figure 4.4 – Variation of sensitivity of THEIA-100 to CP violation due to different $\Delta_{31}m^2$ true values in the cases of NO (left) and IO (right)

7 years of beam exposure are assumed. The shaded area represents the $\pm 3\sigma$ uncertainty in the parameters in question, which have central values denoted by solid lines. No obvious correlation between the sensitivity and the true values of $\Delta_{31}m^2$ can be observed.

this uncertainty is 0.73σ . Other parameter uncertainties, on the other hand, have only limited influence on the sensitivity.

4.2.2 Effect of Variation in Experimental Uncertainties

The assumption of the signal systematic uncertainty to be 2% is an educated guess and requires constraints from the near detectors of the experiment or the results of other similar experiments. In case that the actual uncertainty would deviate from 2%, Figure 4.5 presents the effect on the sensitivity of THEIA to CP violation from different systematic uncertainty assumptions for signals (1% to 3%). For THEIA-25 and THEIA-100 under the standard beam exposure for 7 years, this effect has only limited impact on the sensitivity. However, when an exposure longer than 7 years is considered, or when the upgraded beam with higher power is put to use, the outcome would be more influenced by the variation in systematic uncertainties.

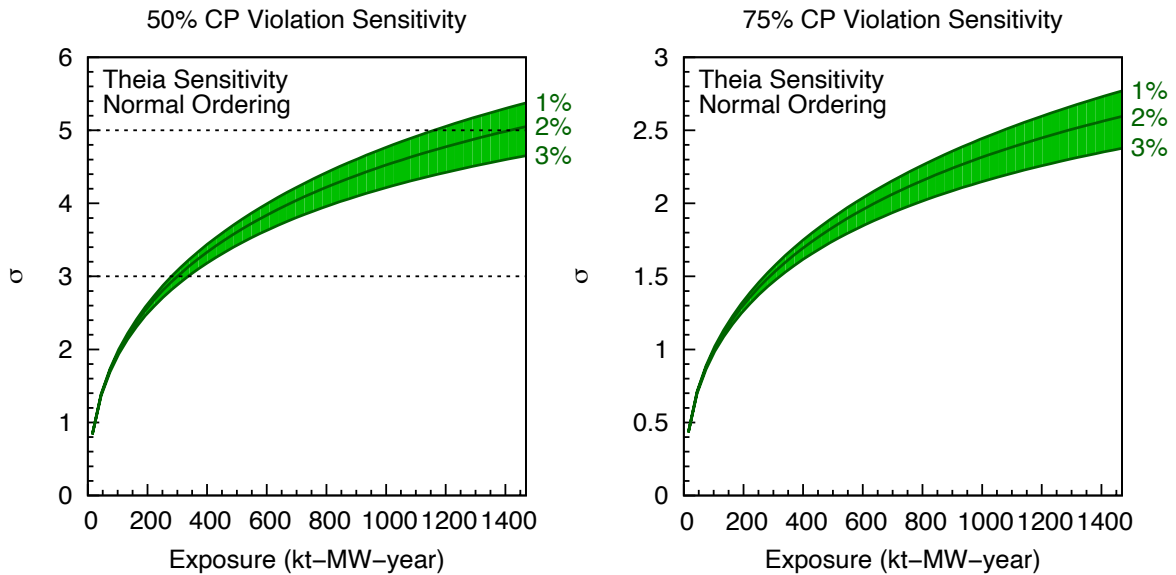


Figure 4.5 – Effect of variation in signal systematic uncertainty on the minimum sensitivity of THEIA to CP violation for 50% (left) and 75% (right) of δ_{CP} parameter space as a function of exposure
Signal systematic uncertainties ranging from 1% to 3% are shown. Assumed here is NO.

A similar examination can be conducted in respect of the error of calorimetric reconstruction of the detected events. One possibility to study this is to adjust the (signal) events s_i in each reconstructed energy bin in a manner that

$$s_i [E_i] \rightarrow s_i \left[(1 + b) \cdot E_i \right], \quad (4.6)$$

where E'_i is the reconstructed neutrino energy in the i th bin, and b is the energy scale error. This adjustment can also be applied to background events b_i . The impact of this error on the sensitivity can be observed in Figure 4.6, where 1% to 5% of energy scale error is studied. While it is clear that this uncertainty can degrade the sensitivity of THEIA, the impact cannot be too serious in this study, since the calorimetric contributions that come from utilizing the detection technique of scintillation light were not included in the simulation.

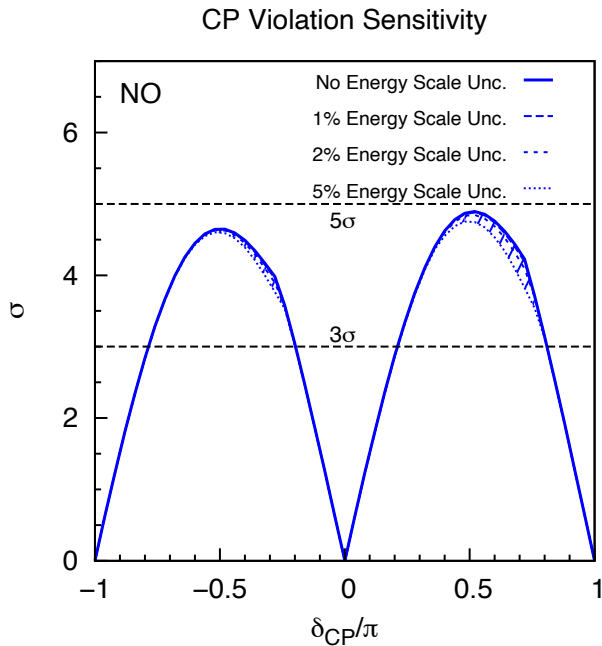


Figure 4.6 – Effect of energy scale uncertainty on the sensitivity of THEIA-100 to CP violation

True NO and 7 years of beam exposure are assumed. The solid line represents the case for no energy scale error, which is also assumed in the production of the result in Figure 4.1. With energy scale errors growing from 1% to 5%, the sensitivity decreases slightly.

4.3 Result: Sensitivity to Neutrino Mass Ordering

The sensitivity of THEIA to determine the correct neutrino mass ordering can also be studied using the analysis procedure with the test statistics mentioned in Subsection 4.1.3. The results are presented in Figure 4.7.

The sensitivity to mass ordering has a different feature from that of the sensitivity to CP violation: a peak of the sensitivity can be found at $\delta_{\text{CP}} = -90^\circ$ in the case of true NO, and at $\delta_{\text{CP}} = 90^\circ$ in the case of true IO. The minimum for each case is then situated at the conjugate CP phase of the peak. This can also be explained by examining the event counts in Table 3.3, where an excess of ν_e events can be observed at $\delta_{\text{CP}} = -90^\circ$ in the case of true NO, and an

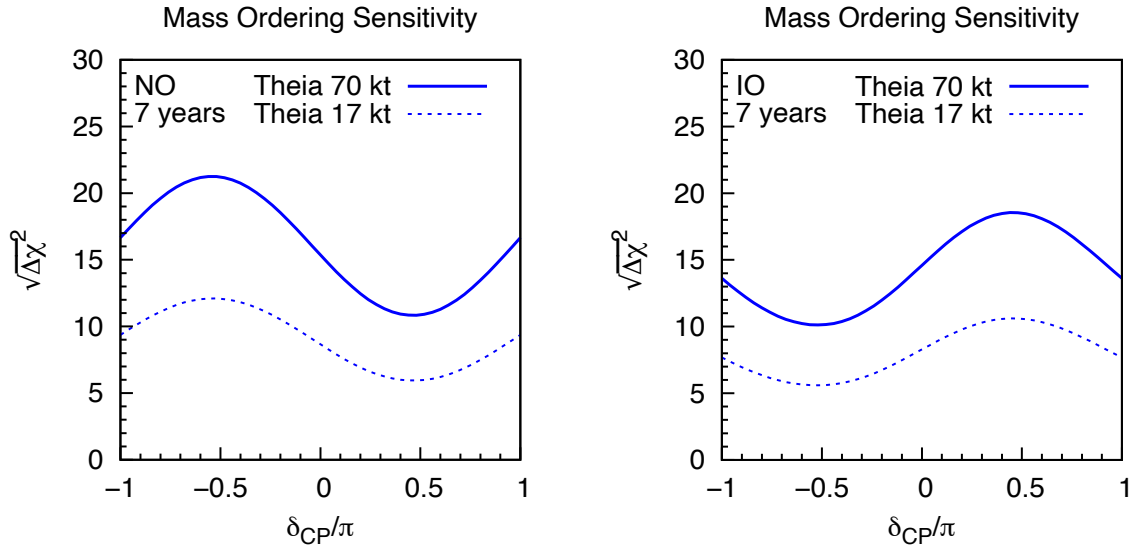


Figure 4.7 – THEIA’s sensitivity to mass ordering in the cases of true NO (left) and true IO (right)

The x-axis indicates the true CP phases. The y-axis is the sensitivity expressed by the square root of the test statistics. Both configurations are considered—THEIA-25 (17-kt fiducial mass, dashed line) and THEIA-100 (70-kt fiducial mass, solid line). 7 years of beam exposure are assumed with equal operation time in FHC and RHC modes.

excess of $\bar{\nu}_e$ events can be observed at $\delta_{CP} = 90^\circ$ in the case of true IO. These excesses present a larger sample size, on which the statistical test takes place, and therefore lead to a higher sensitivity. The same reason goes for explaining the overall higher sensitivity when NO is true, as the smaller interaction cross sections for antineutrinos cause the detected event counts for $\bar{\nu}_e$ in the case of true IO to be lower.

The sensitivity exhibits the ability of the experiment to reject the competing mass ordering hypothesis. As mentioned in Subsection 4.1.3, the special distribution of $\Delta\chi_{MO}^2$ requires a different approach to the interpretation of the sensitivity. This has been studied thoroughly in ref. [66], which gives the following statistical implication. For an experiment that has a sensitivity of $\sqrt{\Delta\chi^2} = 5$, the probability of correct mass ordering determination is 1 (to 3.7 parts per million (ppm) of incorrect determination). When $\sqrt{\Delta\chi^2} = 3$, the probability drops to 98.9%. If the sensitivity is $\sqrt{\Delta\chi^2} = 0$, i.e. the experiment cannot differentiate the results between NO and IO assumptions, the probability of correct mass ordering determination can only be 50%.

From this perspective, both THEIA-25 and THEIA-100 under beam exposure for 7 years can achieve $\sqrt{\Delta\chi^2} > 5$ sensitivity to determination of the correct mass ordering for both mass

orderings and for all possible CP phases. Such a significant performance is mainly contributed by the longer baseline of the experiment, where the asymmetry in the oscillation behaviour between neutrinos and antineutrinos becomes larger with growing matter effect. Hence, THEIA, which performs equivalently to a WCD in the current assumption, is already able to determine the correct mass ordering with high precision when employed at LBNF.

Conclusion

Neutrino physics has come a long way. As of today, theories around the properties of neutrinos have been well established. Nevertheless, questions about these particles still exist—most notably, the possible CP violation in the lepton sector and the neutrino mass ordering. In search of the indications that solve those questions, several neutrino experiments are underway or will be conducted in the near future. THEIA is one of them.

As a hybrid Cherenkov/scintillation detector, THEIA is able to achieve great performance in neutrino detection, where both the directional and calorimetric information of neutrinos will become available in this detector. This is made possible by the development of the novel WbLS and the ultrafast-timing LAPPDs. For such a high-performance detector, the application is envisioned at LBNF in participation of the long-baseline neutrino oscillation experiment, so that THEIA's ability may be utilized in the study of leptonic CP violation and neutrino mass ordering.

In this thesis, the sensitivity studies for this detector were conducted with the GLOBES software, which enables an uncomplicated implementation of simulating any long-baseline experiment. As the performance of THEIA when applied with WbLS and LAPPDs is still a subject of R&D, an assumption on the detector's performance in the experiment has been made, that THEIA has a minimum performance equivalent to that of a WCD, similar to the Super-Kamiokande detector. In this way, a not too optimistic outcome of the simulation was assured.

Using this assumption, the sensitivity of THEIA to leptonic CP violation was revealed with the analytic method of hypothesis testing. From this study, THEIA-100 has a peak sensitivity of 4.9σ in the case of true NO and 5.2σ in the case of true IO, both at the maximally CP-violating phase $\delta_{\text{CP}} = 90^\circ$. For 60% of the δ_{CP} parameter space, THEIA-100 can have a

CONCLUSION

sensitivity of $> 3\sigma$. If IO is realized in nature, THEIA-100 can even reach a sensitivity of $> 5\sigma$ for 20% parameter region around the maximally CP-violating phases. The smaller version of the detector, THEIA-25, has a comparable sensitivity to that of a 10-kt (fiducial) DUNE-FD. The impact from the uncertainties of the oscillation parameters and the systematic parameters on the sensitivity results has also been studied with great effort. Other than from the θ_{23} uncertainty, the influence on the sensitivity turned out to be only minor, partially due to the conservative assumption of the detector's performance.

The sensitivity of THEIA to neutrino mass ordering was also introduced in a lesser extent. Both THEIA-25 and THEIA-100 have the ability to determine the mass ordering with a significance of $\sqrt{\Delta\chi^2} > 5$ regardless of the true CP phase. As for the implication of this sensitivity, recent studies have been considered in presenting a thorough interpretation of the results. The significant performance in the determination of neutrino mass ordering is one of the consequences of THEIA's application at the 1,300-km long LBNF.

Beyond the scope of these studies, several improvements are expected in the future. Once the studies of the implementation of WbLS and LAPPDs on THEIA are available, they can be taken into the account for the sensitivity studies and further increase the detector's sensitivity. This performance test of WbLS and LAPPDs is already underway as part of the Accelerator Neutrino Neutron Interaction Experiment (ANNIE) [68] also at Fermilab. Its results can then directly contribute to the comprehensive design of THEIA. The future upgrade of the neutrino beam from LBNF is also advantageous to the sensitivity by doubling the beam power and thereby reducing the necessary exposure duration for achieving a specific level of sensitivity. From this perspective, the THEIA detector at LBNF will be capable of resolving the puzzles that exist in neutrino physics today.

List of Abbreviations

$0\nu\beta\beta$ decay	neutrinoless double beta decay
ANNIE	Accelerator Neutrino Neutron Interaction Experiment
ASDC	Advanced Scintillation Detector Concept
bf μ	best-fit parameter
BR	branching ratio
BSM	physics beyond the Standard Model
CC interaction	charged-current interaction
CCQE interaction	charged-current quasi-elastic interaction
CKM matrix	Cabibbo–Kobayashi–Maskawa matrix
CL	confidence level
CPV	CP violation
DUNE	Deep Underground Neutrino Experiment
DUNE-FD	DUNE far detectors
DUNE-ND	DUNE near detector complex
Fermilab	Fermi National Accelerator Laboratory
FHC	forward horn current
GERDA	Germanium Detector Array
GLoBES	General Long Baseline Experiment Simulator
GUT	Grand Unified Theory

LIST OF ABBREVIATIONS

IBD	inverse beta decay
IO	inverted mass ordering
IH	inverted mass hierarchy
K2K Experiment	“KEK to Kamioka” Experiment
KamLAND	Kamioka Liquid Scintillator Antineutrino Detector
KATRIN	Karlsruhe Tritium Neutrino Experiment
KEK	Kō Enerugī Kasokuki Kenkyū Kikō (High Energy Accelerator Research Organization)
LAB	linear alkylbenzene
LAPPD	Large Area Picosecond Photo-Detector
LAr	liquid argon
LBNF	Long-Baseline Neutrino Facility
LBNO experiment	long-baseline neutrino oscillation experiment
LSc	liquid scintillator
MC method	Monte Carlo method
MCP	microchannel plate
MI	Main Injector
MiniBooNE	Mini Booster Neutrino Experiment
MINOS	Main Injector Neutrino Oscillation Search
MO	mass ordering
MSW effect	Mikheyev–Smirnov–Wolfenstein effect
NC interaction	neutral-current interaction
NO	normal mass ordering
NH	normal mass hierarchy
NO _{vA}	NuMI Off-Axis ν_e Appearance
NuMI	Neutrinos at the Main Injector
p.d.f.	probability density function
PE	photoelectron

PIP-II	Proton Improvement Plan-II
PMNS matrix	Pontecorvo–Maki–Nakagawa–Sakata matrix
PMT	photomultiplier tube
POT	protons-on-target
ppm	part per million
PPO	2,5-diphenyloxazole
PREM	Preliminary Reference Earth Model
QE	quantum efficiency
R&D	research and development
RENO	Reactor Experiment for Neutrino Oscillation
RHC	reverse horn current
SM	Standard Model
Super-Kamiokande	Super-Kamioka Neutrino Detection Experiment
SURF	Sanford Underground Research Facility
T2K Experiment	“Tokai to Kamioka” Experiment
TTS	transit time spread
WbLS	water-based liquid scintillator
WCD	water Cherenkov detector

LIST OF ABBREVIATIONS

Bibliography

- [1] A. De Angelis and M. Pimenta. *Introduction to Particle and Astroparticle Physics: Multimessenger Astronomy and its Particle Physics Foundations*. Springer, 2nd ed., 2018.
- [2] E. Fermi. Versuch einer Theorie der β -Strahlen. I. *Zeitschrift für Physik*, **A88**(3-4):161-177, 1934.
- [3] C. L. Cowan, Jr., F. Reines, F. B. Harrison, H. W. Kruse and A. D. McGuire. Detection of the Free Neutrino: a Confirmation. *Science*, **124**(3212):103-104, 1956.
- [4] Nobel Foundation. The Nobel Prize in Physics 1995. Retrieved from <https://www.nobelprize.org/prizes/physcis/1995/summary/>.
- [5] D. Galbraith. UX: Standard Model of the Standard Model. Retrieved from <https://davidgalbraith.org/portfolio/ux-standard-model-of-the-standard-model/>.
- [6] D. Karlen. The Number of Light Neutrino Types from Collider Experiments. *Phys. Rev.*, **D86**(1):629, 2012.
- [7] Wikimedia Commons. Right left helicity. 2008.
- [8] D. J. Griffiths. *Introduction to Elementary Particles*. WILEY-VCH, 2008.
- [9] T. D. Lee and C. N. Yang. Question of Parity Conservation in Weak Interactions. *Phys. Rev.*, **104**(1):254-258, 1956.
- [10] S. M. Bilenky. Neutrino oscillation: brief history and present status. 2014.
- [11] S. Lorenz. *Topological Track Reconstruction in Liquid Scintillator and LENA as a Far-Detector in an LBNO Experiment* (dissertation in physics). Retrieved from <https://>

- www.physik.uni-hamburg.de/iexp/gruppe-hagner/pdf/dissertation-slorenz.pdf/, 2016.
- [12] C. Waltham. Teaching neutrino oscillations. *American Journal of Physics*, **72**(6):742-752, 2004.
- [13] P. Alivisatos et al. KamLAND: A Liquid scintillator anti-neutrino detector at the Kamioka site. 1998.
- [14] K2K Collaboration, M. H. Ahn et al. Measurement of Neutrino Oscillation by the K2K Experiment. *Phys. Rev.*, **D74**(7):072003, 2006.
- [15] MINOS, P. Adamson et al. A Study of Muon Neutrino Disappearance Using the Fermilab Main Injector Neutrino Beam. *Phys. Rev.*, **D77**:072002, 2008.
- [16] Daya Bay, X. Guo et al. A Precision measurement of the neutrino mixing angle θ_{13} using reactor antineutrinos at Daya-Bay. 2007.
- [17] Double Chooz, F. Ardellier et al. Double Chooz: A Search for the neutrino mixing angle θ_{13} . 2006.
- [18] RENO, J. Ahn et al. RENO: An Experiment for Neutrino Oscillation Parameter θ_{13} Using Reactor Neutrinos at Yonggwang. 2010.
- [19] T2K Collaboration, K. Abe et al. The T2K Experiment. *Nucl. Instrum. Meth.*, **A659**:106, 2011.
- [20] NOvA Collaboration, D. Ayres et al. NOvA: Proposal to build a 30 kiloton off-axis detector to study $\nu_{\mu} \rightarrow \nu_e$ oscillations in the NuMI beamline. 2005.
- [21] I. Esteban, M. C. Gonzalez-Garcia, A. Hernandez-Cabezudo, M. Maltoni and T. Schwetz. Global analysis of three-flavour neutrino oscillations: synergies and tensions in the determination of θ_{23} , δ_{CP} , and the mass ordering. *Journal of High Energy Physics*, **2019**(106), 2019.
- [22] NuFIT 4.0 (2018). Retrieved from <http://www.nu-fit.org/>.
- [23] Planck Collaboration. Planck 2018 results. VI. Cosmological parameters. *Astronomy & Astrophysics*, **641**(A6):A6, 2020.
- [24] M. Tanabashi et al. (Particle Data Group). Review of Particle Physics: Neutrino Properties. *Phys. Rev.*, **D98**:030001, 2018.
- [25] The KATRIN Collaboration. Direct neutrino-mass measurement with sub-electronvolt sensitivity. *Nat. Phys.*, **18**:160-166, 2022.

- [26] E. Majorana. Teoria simmetrica dell'elettrone e del positrone. *Il Nuovo Cimento*, **14**(4):171-184, 1937.
- [27] L. Oberauer, A. Ianni, A. Serenelli. *Solar neutrino physics: the interplay between particle physics and astronomy*. Wiley-VCH, 2020.
- [28] Wikimedia Commons. Double beta decay feynman. 2009.
- [29] GERDA Collaboration, M. Agostini, G. R. Araujo, A. M. Bakalyarov, M. Balata, I. Barabanov, L. Baudis, C. Bauer, E. Bellotti. Final Results of GERDA on the Search for Neutrinoless Double- β Decay. *Phys. Rev.*, **125**(25):252502, 2020.
- [30] MiniBooNE Collaboration, A. A. Aguilar-Arevalo, B. C. Brown, L. Bugel, G. Cheng, J. M. Conrad, R. L. Cooper et al. Observation of a significant excess of electron-like events in the MiniBooNE short-baseline neutrino experiment. *Phys. Rev.*, **121**(22):221801, 2018.
- [31] F. P. An, A. B. Balantekin, H. R. Band, W. Beriguete, M. Bishai, S. Blyth et al. Search for a light sterile neutrino at Daya Bay. *Phys. Rev.*, **113**(14):141802, 2014.
- [32] M. Drewes. The phenomenology of right handed neutrinos. *International Journal of Modern Physics*, **E22**(8):1330019-1330593, 2013.
- [33] W. R. Leo. *Techniques for Nuclear and Particle Physics Experiments*. Springer, 2nd ed., 1994.
- [34] J. B. Birks. Scintillations from Organic Crystals: Specific Fluorescence and Relative Response to Different Radiations. *Proc. Phys. Soc.*, **A64**(10):874-877, 1951.
- [35] J. D. Jackson. *Classical electrodynamics*. Wiley, 3rd ed., 1999.
- [36] S. G. Warren. Optical constants of ice from the ultraviolet to the microwave. *Appl. Opt.*, **23**:1206, 1984.
- [37] G. M. Hale and M. R. Querry. Optical Constants of Water in the 200-nm to 200- μ m Wavelength Region. *Appl. Opt.*, **12**:555, 1973.
- [38] LENA Collaboration, M. Wurm et al. The next-generation liquid-scintillator neutrino observatory LENA. *Astropart. Phys.*, **35**:685, 2012.
- [39] M. Antonello et al. Detection of Cherenkov light emission in liquid argon. *Nucl. Instrum. Meth.*, **A516**:348, 2004.

- [40] T2K Collaboration, K. Abe et al. Constraint on the matter–antimatter symmetry-violating phase in neutrino oscillations. *Nature*, **580**(7803):339-344, 2020.
- [41] Hamamatsu Photonics K. K. *Photomultiplier Tubes - Basics and Applications*. Hamamatsu Photonics K. K., 3rd ed., 2007.
- [42] A. Lyashenko et al. Performance of Large Area Picosecond Photo-Detectors (LAPPD™). *Nucl. Instrum. Meth.*, **A958**:162834, 2020.
- [43] A. Elagin. *Large-Area Picosecond Photo-Detectors* (FroST-II Workshop, Mainz). Retrieved from https://indico.mitp.uni-mainz.de/event/83/contributions/2498/attachments/1979/2083/AElagin_FroST_Oct2016_v2.pdf, 2016.
- [44] THEIA Collaboration, M. Askins et al. THEIA: an advanced optical neutrino detector. *Eur. Phys. J.*, **C80**(5):416, 2020.
- [45] J. Alonso et al. Advanced scintillation detector concept. 2014.
- [46] J. Brack, B. Delgado, J. Dhooghe, J. Felde, B. Gookin, S. Grullon, J. Klein, R. Knapik, A. LaTorre, S. Seibert, K. Shapiro, R. Svoboda, L. Ware and R. Van Berg. Characterization of the Hamamatsu R11780 12 inch Photomultiplier Tube. *Nucl. Instrum. Meth.*, **A712**:162, 2013.
- [47] J. Strait et al. Long-Baseline Neutrino Facility (LBNF) and Deep Underground Neutrino Experiment (DUNE) Conceptual Design Report Volume 3: Long-Baseline Neutrino Facility for DUNE June 24, 2015. 2016.
- [48] R. Acciarri et al. Long-Baseline Neutrino Facility (LBNF) and Deep Underground Neutrino Experiment (DUNE) Conceptual Design Report Volume 2: The Physics Program for DUNE at LBNF. 2016.
- [49] DUNE Collaboration. Deep Underground Neutrino Experiment. Retrieved from <https://www.dunescience.org/>.
- [50] M. Tanabashi et al. (Particle Data Group). Review of Particle Physics: Mesons. *Phys. Rev.*, **D98**:030001, 2018.
- [51] M. Tanabashi et al. (Particle Data Group). Review of Particle Physics: Leptons. *Phys. Rev.*, **D98**:030001, 2018.
- [52] S. Kopp. Accelerator neutrino beams. *Physics Reports*, **439**(3):101-159, 2007.
- [53] DUNE Collaboration, T. Alion et al. Experiment Simulation Configuration Used in DUNE CDR. 2016.

- [54] A. M. Dziewonski and D. L. Anderson. Preliminary reference Earth model. *Physics of the Earth and Planetary Interiors*, **25**(4):297-356, 1981.
- [55] F. D. Stacey. *Physics of the earth*. Wiley, 2nd ed., 1977.
- [56] M. D. Messier. *Evidence for neutrino mass from observations of atmospheric neutrinos with Super-Kamiokande* (dissertation in physics). Retrieved from <http://budoe.bu.edu/~messier/thesis/messier-thesis.pdf>, 1999.
- [57] E. A. Paschos and J. Y. Yu. Neutrino interactions in oscillation experiments. *Phys. Rev.*, **D65**:033002, 2002.
- [58] P. Huber, M. Lindner and W. Winter. Superbeams versus neutrino factories. *Nucl. Phys.*, **B645**:3-48, 2002.
- [59] T2K Collaboration, Y. Itow et al. The JHF-Kamioka neutrino project. 2001.
- [60] P. Huber, M. Lindner and W. Winter. Simulation of long-baseline neutrino oscillation experiments with GLoBES (General Long Baseline Experiment Simulator). *Comput. Phys. Commun.*, **167**:195, 2005.
- [61] P. Huber, J. Kopp, M. Lindner, M. Rolinec and W. Winter. New features in the simulation of neutrino oscillation experiments with GLoBES 3.0: General Long Baseline Experiment Simulator. *Comput. Phys. Commun.*, **177**:432, 2007.
- [62] G. Cowan, K. Cranmer, E. Gross and O. Vitells. Asymptotic formulae for likelihood-based tests of new physics. *Eur. Phys. J.*, **C71**:1554, 2011.
- [63] H. Nunokawa, S. J. Parke and J. W. Valle. CP Violation and Neutrino Oscillations. *Prog. Part. Nucl. Phys.*, **60**:338-402, 2008.
- [64] DUNE Collaboration, A. Abed Abud et al. Deep Underground Neutrino Experiment (DUNE) Near Detector Conceptual Design Report. *Instrument 5*, **4**:31, 2021.
- [65] LBNE Collaboration, C. Adam et al. The Long-Baseline Neutrino Experiment: Exploring Fundamental Symmetries of the Universe. 2013.
- [66] X. Qian, A. Tan, W. Wang, J. Ling, R. McKeown et al. Statistical Evaluation of Experimental Determinations of Neutrino Mass Hierarchy. *Phys. Rev.*, **D86**:113011, 2012.
- [67] M. Blennow, P. Coloma, P. Huber and T. Schwetz. Quantifying the sensitivity of oscillation experiments to the neutrino mass ordering. *JHEP*, **1403**:028, 2014.

BIBLIOGRAPHY

- [68] ANNIE Collaboration, A. R. Back et al. Accelerator Neutrino Neutron Interaction Experiment (ANNIE): Preliminary Results and Physics Phase Proposal. 2017.

Acknowledgements

For the production of this thesis, I would like to thank the whole working group of Prof. Dr. Caren Hagner. Without their support, the completion of this work would not be possible. Especially to those who have provided their advice in the construction of the texts—Vidhya Thara Hariharan, Dr. Tamer Tolba, Malte Stender and Rosmarie Wirth, I would thank you all from the bottom of my heart. Your input has been very important to me, as it gave me motivation again and again in self-improvement.

As for the persons who introduced me to this research topic—Prof. Dr. Caren Hagner and Dr. Björn Wonsak, I would thank you both for your guidance in the methods of conducting research. For a research beginner like me, this means a lot. I would also like to thank Prof. Dr. Michael Wilking and Prof. Dr. Elizabeth Worcester in the US, who have assisted me in the operation of the GLOBES software and the implementation of the analysis methods.

To both of my supervisors—Dr. Daniel Bick and Prof. Dr. Michael Wurm, I would like to express my most sincere gratitude. To “Michi,” I would like to thank you for your support for my work and the agreement to be a reviewer for this thesis, which has been a huge relief for me at the time. As for Daniel, I somehow could not thank you enough, as you have helped me with every problem I had, whether it be coding-related questions or organizational issues. You are and have been always a person of good nature to me. I am really grateful to be able to work with you.



Universität Hamburg

DER FORSCHUNG | DER LEHRE | DER BILDUNG

Eidesstattliche Erklärung

Ich versichere, dass ich die beigelegte schriftliche ~~Bachelorarbeit/Masterarbeit~~ selbstständig angefertigt und keine anderen als die angegebenen Hilfsmittel benutzt habe.

Alle Stellen, die dem Wortlaut oder dem Sinn nach anderen Werken entnommen sind, habe ich in jedem einzelnen Fall unter genauer Angabe der Quelle deutlich als Entlehnung kenntlich gemacht. Dies gilt auch für alle Informationen, die dem Internet oder anderer elektronischer Datensammlungen entnommen wurden. Ich erkläre ferner, dass die von mir angefertigte ~~Bachelorarbeit/Masterarbeit~~ in gleicher oder ähnlicher Fassung noch nicht Bestandteil einer Studien- oder Prüfungsleistung im Rahmen meines Studiums war. Die von mir eingereichte schriftliche Fassung entspricht jener auf dem elektronischen Speichermedium.

Ich bin damit ~~(nicht)~~ einverstanden, dass die ~~Bachelorarbeit/Masterarbeit~~ veröffentlicht wird.

Hamburg 30.03.2023

李 幸 頌

Ort, Datum

Unterschrift